Mississippi State University
Scholars Junction

Theses and Dissertations | Theses and Dissertations

12-13-2019

Flexural bending test of topology optimization additively manufactured parts

Mohammed Afify

Follow this and additional works at: https://scholarsjunction.msstate.edu/td

Recommended Citation
Afify, Mohammed, "Flexural bending test of topology optimization additively manufactured parts" (2019). *Theses and Dissertations*. 2311.
https://scholarsjunction.msstate.edu/td/2311

This Graduate Thesis - Open Access is brought to you for free and open access by the Theses and Dissertations at Scholars Junction. It has been accepted for inclusion in Theses and Dissertations by an authorized administrator of Scholars Junction. For more information, please contact scholcomm@msstate.libanswers.com.

Flexural bending test of topology optimization additively manufactured parts

By

Mohammed Afify

A Thesis
Submitted to the Faculty of
Mississippi State University
in Partial Fulfillment of the Requirements
for the Degree of Master of Science
in Aerospace Engineering
in the Department of Aerospace Engineering

Mississippi State, Mississippi

December 2019

Copyright by

Mohammed Afify

2019

Flexural bending test of topology optimization additively manufactured parts

By

Mohammed Afify

Approved:

_____

Davy M. Belk
(Major Professor)

_____

Bian Linkan
(Committee Member)

_____

Haley R. Doude
(Committee Member)

_____

Yeqing Wang
(Committee Member)

_____

David S. Thompson
(Graduate Coordinator)

_____

Jason M. Keith
Dean
Bagley College of Engineering

Name: Mohammed Afify

Date of Degree: December 13, 2019

Institution: Mississippi State University

Major Field: Aerospace Engineering

Major Professors: Davy M. Belk

Title of Study: Flexural bending test of topology optimization additively manufactured parts

Pages in Study: 104

Candidate for Degree of Master of Science

The aim of this work is to model, manufacture, and test an optimized Messerschmitt-Bölkow-Blohm beam using additive manufacturing. The implemented method is the Solid Isotropic Material with Penalization of a minimum compliance design. The Taubin smoothing technique was used to attenuate geometric noise and minimize the formation of overhanging angles and residual stresses due to the thermal activity of the selective laser melting process. The optimized model required examination and repair of local errors such as surface gaps, non-manifold vertices, and intersecting facets. A comparison between experimental and numerical results of the linear elastic regimes showed that the additively manufactured structure was less stiff than predicted. Potential contributors are discussed, including the formation of an anisotropic microstructure throughout the layer-by-layer melting process. In addition, the effect of selective laser melting process on the mechanical properties of stainless steel 316l-0407 and its influence on structural performance was described.

DEDICATION

I dedicate this work to my beloved family, friends and all the people who made this academic experience enriching and effectual. During my academic career, I had the chance to meet a variety of inspiring and devoted faculty members that helped me evolve intellectually and made me who I am today.

ACKNOWLEDGEMENTS

This thesis is related to the achievement of a master's degree in Aerospace Engineering at the Aerospace Engineering Department, Mississippi State University.

First, I want to thank my supervisors Dr. Davy Belk and Dr. Bian Linkan for their assistance throughout this work. Also, I want to thank Dr. Haley Doude and Dr. Rhatan Jha for making this thesis possible regarding their help and advice throughout the thesis. This research project was beneficial in terms of the devoted knowledge related to both topology optimization and additive manufacturing.

Finally, I want to thank my family for their counseling and support. In the meantime, I want to thank my colleagues for the amazing academic experience we had at Mississippi State University.

Starkville, December 2019

Afify Mohammed

TABLE OF CONTENTS

LIST OF TABLES

LIST OF FIGURES

NOMENCLATURE

ρ	Density
u	Displacement
K	Global Stiffness matrix
F	Global Load vector
p	Penalization
E	Young Modulus Elasticity
v	Poisson's ratio
U	Space of admissible displacements
E_e^0	Original material elastic modulus
E_{ad}	Class of allowable stiffness tensors
K_e	Element stiffness matrix
E_{min}	Stiffness of void material
ρ_e^p	Artificial density at power p
$\rho(x)$	Density function
E_e	New artificial elastic modulus of the eth element
$V(\rho)$	Available material volume
V_0	Volume of the design domain.
V_f	Volume fraction.

q	Gray-scale factor
I	Moment of inertia
P	Load
L	Distance between supports
δ	Deflection

CHAPTER I

BACKGROUND

1.1 Introduction

Nowadays, additive manufacturing has become a necessary industrial process showing a tremendous capacity in printing complex models within a predefined timeslot. Additive manufacturing grasped its importance based on its involvement in a variety of applications such as automotive, aerospace, and biomedical engineering. Additive manufacturing uses 3D-printing process in order to get the desired products. This technology operates using a layer-by-layer deposition; it is a superposition of a binder material onto a powder bed. The models before printing are on either STL or FDM format depending on the technology used. The integration of topology optimization concept into the additive manufacturing process improved the rate of manufacturability and enhanced the accuracy of the designed models by reaching optimal shapes of structures via weight reduction. The actual aerospace industry implements the additive manufacturing process throughout the fabrication of mechanical parts, which constitute the main subparts of aircrafts such as wings, fuselages. Additive manufacturing builds mechanical parts using a variety of metallic powders [1] (Gibson et al. 2015). The primary concern of structural optimization is to achieve an optimal material distribution within a predefined design domain of the optimization problem that would support a specific load aiming to maximize the overall stiffness within the structure. Also, structural optimization is composed of three categories based on the established parametric configuration of the design. The material distribution method enables

the integration of the three optimization categories concurrently within the design process. Topology optimization problem includes design specifications of the solid such as the number and the size of the holes within the domain. Also, it involves the connectivity of the domain [2] (Christensen et al., 2008). Topology optimization is widely spread within the aerospace industry in the improvement of intricate designs enabling engineers to examine multiple approaches. Since topology optimization enables engineers to manufacture complex structures, it has become necessary to integrate this tool within the additive manufacturing process. Multiple difficulties could encounter an additive manufacturing process, such as overhang and anisotropy [3] (Clausen, 2016).

1.2 Objectives

The main goals of the thesis are the following:

- Optimize and manufacture a Messerschmitt-Bölkow-Blohm beam combining SIMP topology optimization method and additive manufacturing using the selective laser melting process.
- Apply Taubin mesh smoothing technique to the optimized models to minimize the formation of overhang angles and residual stresses as well as illustrate its effect on the structural performance of the smoothed models in terms of geometry preservation.
- Evaluate the bending mechanism of additively manufactured parts using a three-point bending test.
- Discuss the anisotropic behavior of additively manufactured parts and compare between numerical and experimental results as well as emphasize the effect of the selective laser melting process on mechanical properties such as Young's modulus, hardness, and yield strength.

1.3 Outline

The thesis project is composed of seven parts; each part focuses on a specific topic. The first chapter invokes an illustration of topology optimization and additive manufacturing as well as the outcome of their combination. A brief description of the finite element method is mentioned to highlight its importance regarding structural optimization. Throughout the second chapter, a detailed study of topology optimization characteristics is cited to elucidate the primary function of the method and its conditions — an explanation of the solid isotropic material with penalization through its theoretical formulation and its physical interpretation as well as the concept of the minimum compliance design. Besides, optimization algorithms such as optimality criteria method, method of moving asymptotes and sequential quadratic programming are illustrated using mathematical formulations and algorithms. Both the checkerboarding problem and the gray-scale filter are emphasized. In the third chapter, the optimization code is presented by defining its characterizing features and the steps of the optimization process. Results of the optimization code are analyzed under the applied boundary conditions and external loads. The objective function is discussed as well as the number of iterations that lead to the result. In the fourth chapter, the Taubin smoothing method is illustrated using both mathematical overview and physical characterization of the scheme. The smoothing technique is applied to the optimized model using defined parameters. In the fifth chapter, local errors within the resulting mesh, such as surface gaps, non-manifold vertices, and intersecting facets are repaired. In the sixth chapter, a detailed finite element analysis is used to show the behavior of the optimized model prior mechanical testing comprising the assigned mesh, boundary conditions, applied load and material properties as well as the obtained results such as stress distribution, deformation, and the occurred deflection. In the seventh chapter, a detailed description of the three-point bending test showing the apparatus and the

supports used throughout the experiment. The internal supports of the printed models are cleaned and prepared for the test. After the execution of the three-point bending test, the load-deflection data are gathered from the testing machine for further analysis. Based on the results obtained from the numerical model using a static linear elastic simulation, the slope of the load-deflection analysis is used to set a comparison between the numerical model and the experimental model. The comparative analysis showed a significant difference in flexural stiffness between the numerical and experimental results; this difference is discussed in detail for a profound understanding of the flexural bending behavior of additively manufactured parts.

Potential contributors are discussed, including the formation of an anisotropic microstructure throughout the layer-by-layer melting process. Also, the effect of selective laser melting process on the mechanical properties of stainless steel 316l-0407 and its influence on structural performance was described.

Figure 1.1 Workflow of the thesis

1.4 Finite Element Method

Finite element method is a numerical technique well known for solving structural engineering problems; the formulation of the method is expressed through a multiplicity of an algebraic set of equations, which depicts the behavior of certain variables throughout a design domain. The finite element method is employed to determine the objective function of the topology optimization problem as a function of the design variable. It is necessary to determine the displacement corresponding to the specified design variable [4]. In the finite element method, the design domain is subdivided into small components called finite elements [5]. After discretizing the domain, each element is supposed to have a set of results that describe the behavior of the problem locally. Finally, the results obtained at each finite element are gathered into a set of equations that models the entire behavior of the problem [6]. In most engineering problems, it is inevitable to implement numerical approaches to solve topology optimization structures. Hence, most optimization algorithms use the finite element method, such as SIMP and BESO. It is perceivable that the finite element method is implemented within topology optimization codes. Although the finite element method has multiple advantages, still it has some significant drawbacks such as stability and boundary representations.

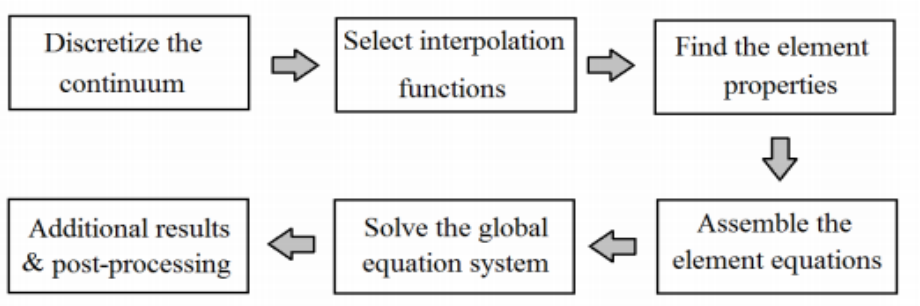

Figure 1.2 Finite element analysis workflow [6]

CHAPTER II

INTRODUCTION TO TOPOLOGY OPTIMIZATION

Topology optimization aims to find an optimal material distribution for a defined volume fraction in a design domain. The optimality of material distribution is quantified by its overall stiffness, meaning that a high stiffness structure possesses an optimal material distribution within its design domain. Throughout this approach, design specifications such as internal and external boundary configurations are included within the optimization process. Moreover, topology optimization applies to both continuum and discrete structures. Since the material distribution method is the foundation of topology optimization, the objective is to develop structural designs by minimizing objective functions under specific boundary conditions and volume constraints.

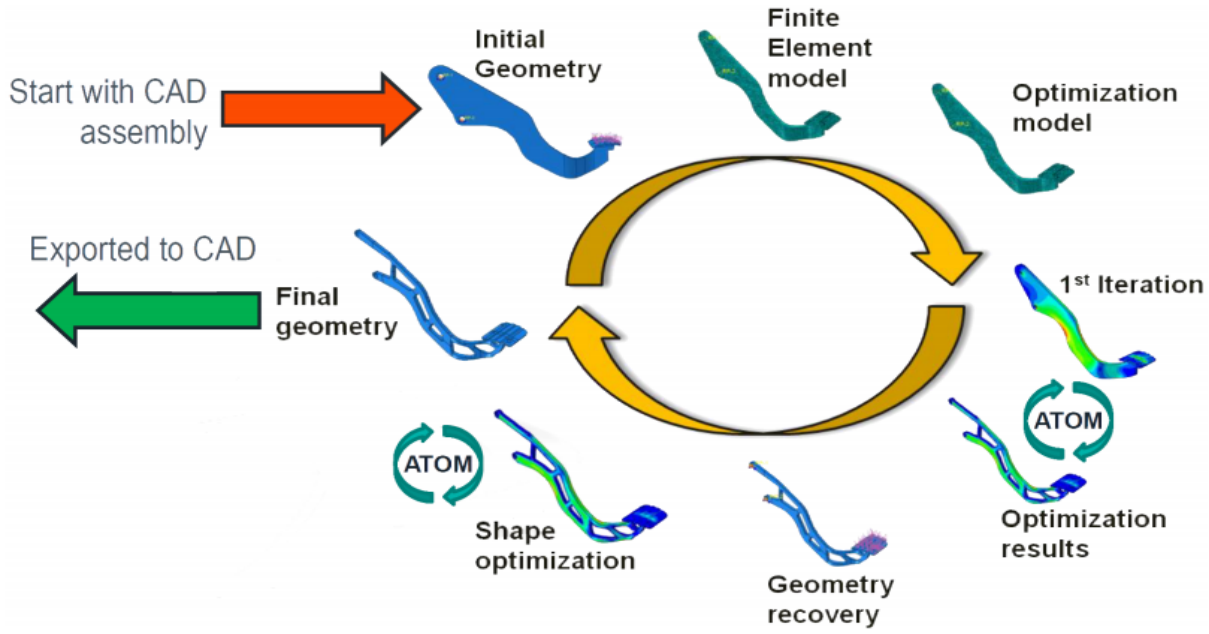

Figure 2.1 Steps of topology optimization [7]

Furthermore, structural optimization is composed of three categories, such as sizing optimization, shape optimization, and topology optimization. Each structural optimization is defined as follow:

- **Sizing optimization:** Optimizes the material's distribution within the thickness of elastic structures. Furthermore, the sizing problem is characterized by the fact that the design domain of the model and its state variables are deduced and specified within the optimization process.
- **Shape optimization:** Aims to obtain an optimal shape of the design domain. In this kind of problems, the design domain is taken to be the design variable, which converges to an optimized shape domain at the end of the process.
- **Topology optimization:** This type of optimization problem includes design specifications of the solid such as the number and the size of the holes within the domain. Also, it involves the connectivity of the domain.

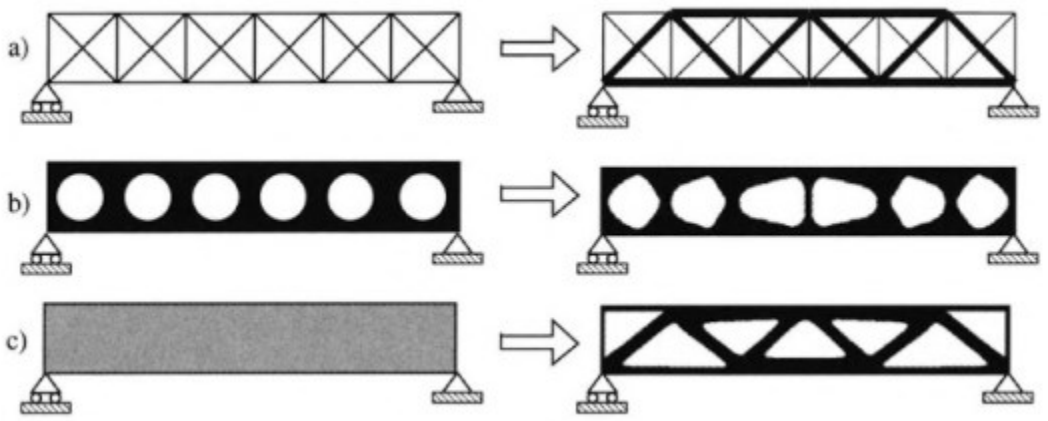

Figure 2.2 (a) Sizing optimization, (b) Shape optimization, (c) Topology optimization [8]

Optimizing designs in terms of stiffness requires an objective function that minimizes the total strain energy within a predefined domain under the application of body forces (Bendsøe,1998) [9]. In multiple topology optimization problems, it is necessary to specify both structural parameterizations of the design domain and the state variables related to the objective function.

2.1 Minimum compliance design

The minimum compliance problem aims to obtain design variables that minimize the structure's deflection using specific boundary conditions and loads. The general form of compliance is formulated as follows [10]:

$$C(\rho) = F^T U(\rho) \tag{2.1}$$

F: vector of nodal force.

U: vector of nodal displacement.

ρ: density distribution.

The formulation of the minimum compliance problem is as follows:

$$min_\rho \ C(\rho) = F^T U(\rho)$$

constraints: $$\frac{V(\rho)}{V_0} = V_f \quad (2.2)$$

$$F = KU$$

$$0 < \rho_{min} \leq \rho_e \leq 1$$

$V(\rho)$: available material volume.

V_0: volume of the design domain.

V_f: volume fraction.

K: stiffness.

Based on the relation between the nodal force and the compliance:

$$C(\rho) = F^T U$$

$$F = KU \quad (2.3)$$

$$C(\rho) = U^T K U$$

Based on the equation (2.3), the global compliance is formulated as follows:

$$C(\rho) = \sum_{e=1}^{N} u_e^T K_e u_e \quad (2.4)$$

u_e: element displacement vector.

K_e: element stiffness matrix.

N: number of elements of the discretized design domain.

2.2 Solid Isotropic Material with Penalization – SIMP

A common optimization technique called solid isotropic material with penalization uses a density-based approach to reach an optimal material distribution within a design domain. This method is based on the developed work of Bendsøe and Kikushi [11] on the homogenization method.

The SIMP method depends on the following relation:

$$E_e(\rho_e) = \rho_e^p(E_0), \qquad 0 < \rho_{min} \leq \rho_e \leq 1 \qquad (2.5)$$

ρ_e: relative element density.

E_e: element Young's modulus of the solid material.

ρ_{min}: relative element density of the void material.

p: penalization power, $p > 1$.

The relative element density ρ_{min} is different from zero to prevent singularity of the element stiffness matrix.

The modified SIMP is formulated as follows:

$$E_e(\rho_e) = E_{min} + \rho_e^p(E_0 - E_{min}), \qquad \rho_e \in [0,1] \qquad (2.6)$$

E_{min}: Young's modulus of the void material.

The Young's modulus of the void material E_{min} is different from zero to prevent singularity of the element stiffness matrix.

The global stiffness matrix K is formulated as follows:

$$K(\rho) = \sum_{e=1}^{N} K_e(\rho_e) \qquad (2.7)$$

Also, the element stiffness matrix K_e is formulated as follows:

$$K_e(\rho) = E_e(\rho_e)k_e^0 \qquad (2.8)$$

k_e^0: element stiffness matrix of an element with a unit Young's modulus.

Based on the formulation, k_e^0 do not depend on the relative element density ρ_e but it is related to Poisson's ratio and the type of element.

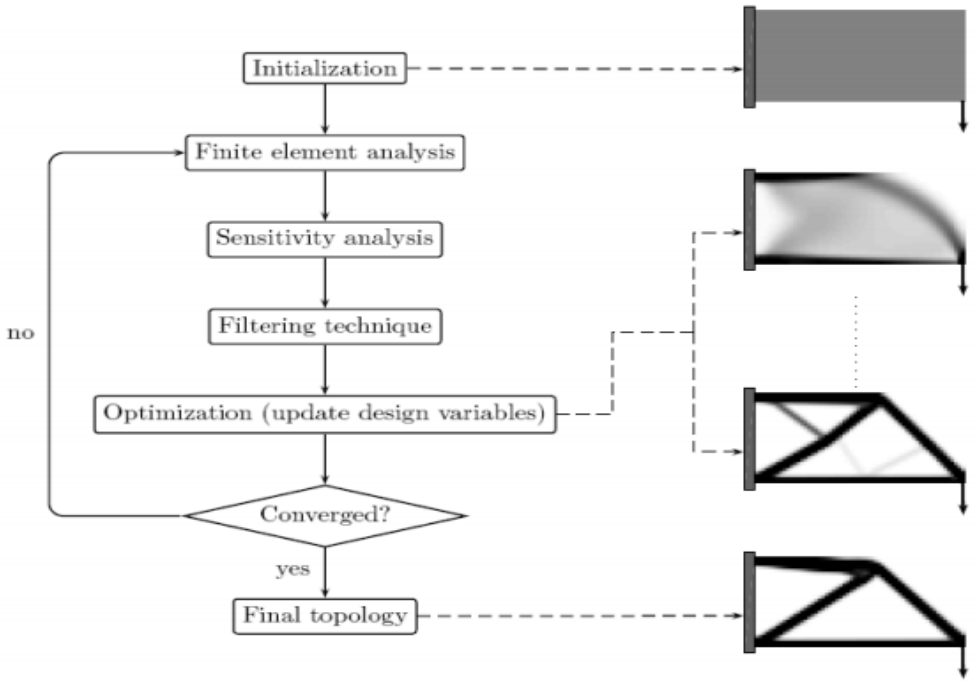

Figure 2.3 Workflow of the SIMP method [12].

2.3 Optimization Algorithms

Since minimum is a non-linear programming problem, it can be solved using sequential convex approximations such as the method of moving asymptotes and the sequential quadratic programming [13]. The objective of these methods is to obtain an enhanced design x^{k+1} using a convex approximation based on an initial problem x^{k}. The most used algorithms are optimality criteria method, sequential quadratic programming and the method of moving asymptotes. These methods were implemented in the topology optimization code used throughout this work.

2.4 Checkerboard Patterns

The checkerboard filtering is implemented to refine the converged topology optimization result by avoiding the formation of alternating solid-void regions. The checkerboarding pattern is generally induced throughout the conservation of higher stiffness elements based on the finite element analysis generating an alternation of relative densities [14]. In terms of fabrication, these patterns cause geometric non-linearities lowering the overall structural integrity of solid models. In order to solve this issue, higher order finite elements are used in the optimization problem to attenuate the formation of severe checkerboarding patterns.

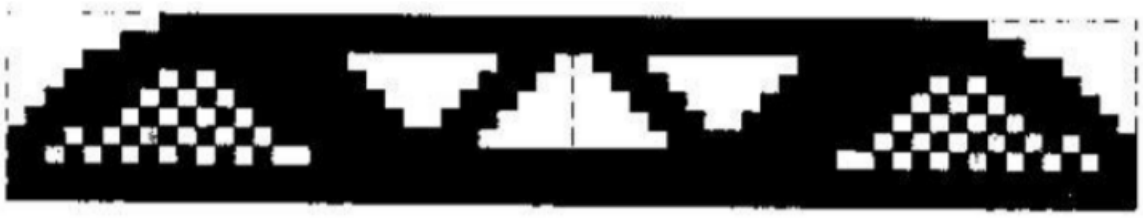

Figure 2.4 Checkerboard pattern [15].

2.5 Gray-scale Filter

A new method is introduced to achieve white-black regions in 3D topology optimization applications by (Groenwold and Etman, 2009). (Liu and Tovar, 2014) implemented the filter in their MATLAB optimization code. The filter uses an exponent q to attain the white-black regions in the optimization problem. The standard optimality criteria method used is a special case of q=1.

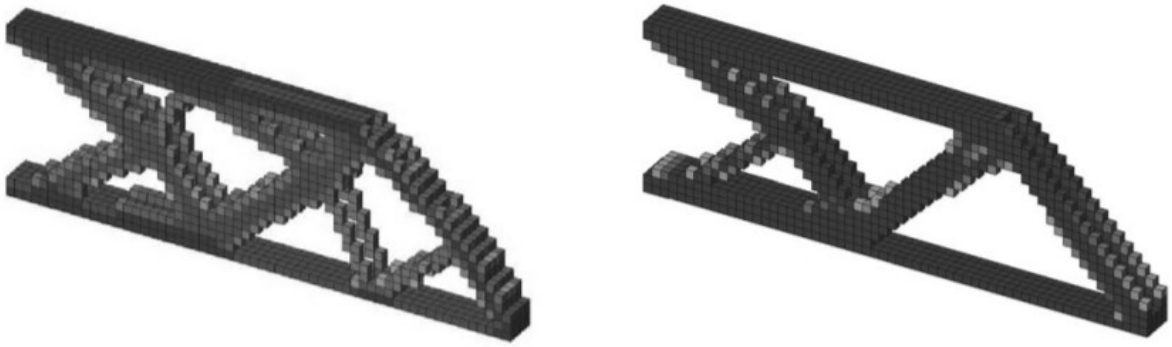

Figure 2.5 Left optimized design using density filter, right optimized design using density filter and gray scale filter [16].

CHAPTER III

NUMERICAL IMPLEMENTATIONS OF SIMP METHOD USING MATLAB 3D CODE

A topology optimization code for 3D structures, using a fastidious approach to solve minimum compliance problems based on the modified SIMP. This latter is employed to optimize predefined design domains based on specific boundary conditions and external loads. In this part, a minimum compliance problem is established to obtain optimal material distribution. The optimization code uses a density-based approach instead of the homogenization method. The density-based approach uses a power-interpolation function to determine mechanical properties such as stiffness tensor within a design domain [17]. In fact, it is difficult to manufacture optimized models using the homogenization theory, since the "gray" regions obtained within the optimized designs have microscopic length-scale holes that are complex to produce [18]. Moreover, the optimization code uses a density filter to mitigate numerical problems such as checkerboard patterns, mesh-dependency, and local minima [19]. The following part describes the steps accomplished throughout the optimization process such as degrees of freedom of a discretized domain, boundary conditions at specific nodes, and the location of the applied load. In addition, the objective function of the beam is discussed based on the number of iterations prior convergence. The used code is courtesy of (Liu and Tovar, 2014).

3.1 SIMP Approach

As mentioned in the previous chapters, the topology optimization method used is SIMP. This method implements a density-based approach to solve structural optimization problems. The SIMP method is widely used in most topology optimization applications.

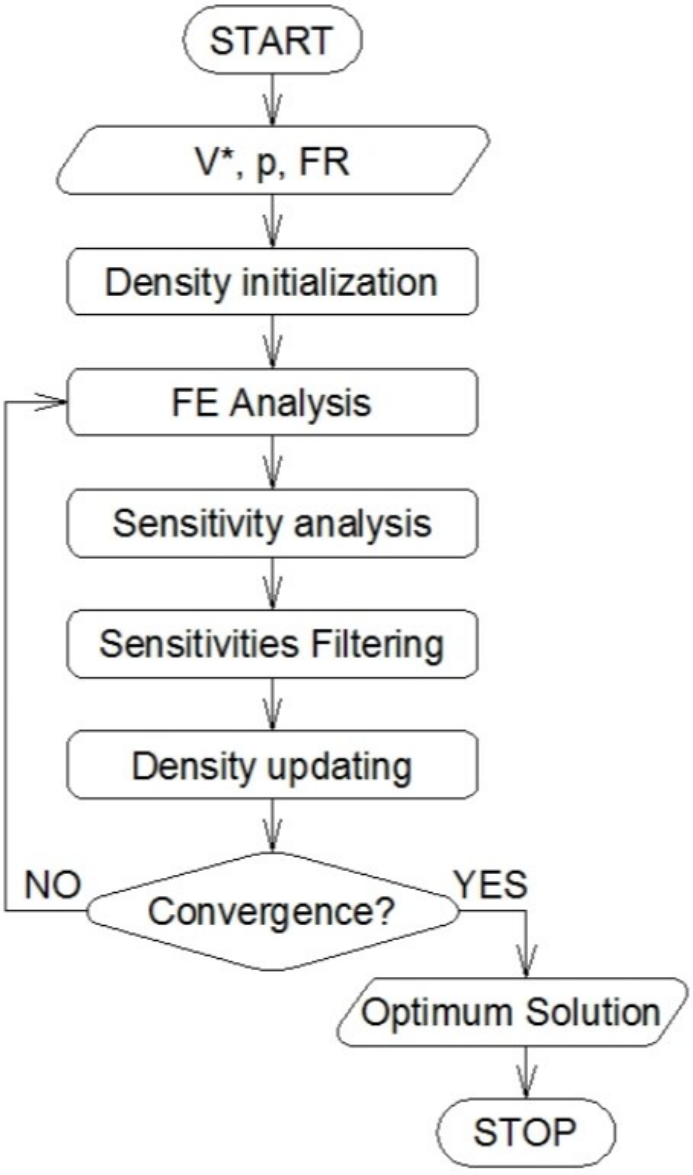

Figure 3.1 SIMP workflow [20]

3.2 Initialization Parameters

Throughout the SIMP algorithm implemented within Liu and Tovar's code, several parameters are set by the user to define the requirements of the optimization problem. The command line used in MATLAB is the following:

top3d14(nelx, nely, nelz, volfrac, penal, q, rmin)

- **nelx:** number of elements in the x-direction.
- **nely:** number of elements in the y-direction.
- **nelz:** number of elements in the z-direction.
- **volfrac:** volume fraction; the amount of volume that is preserved from the initial structure prior optimization.
- **penal:** the penalization factor of the SIMP method, p =3.
- **q:** gray-scale penalty factor, q =2.
- **rmin:** filter radius, the distance between two neighboring elements that is considered by the sensitivity [21].

The elemental densities ρ_e are initiated using the same value, which the volume fraction. Using the modified SIMP approach, the virtual densities are converted to physical material properties. The defined material properties are:

- E_{min}: elastic modulus of the void material [22].
- E_0: elastic modulus of the applied material.

The elastic modulus and Poisson's ratio are used in the finite element analysis.

3.3 Node Coordinates

Throughout the optimization code, the coordinates of each node within the discretized domain must be defined to assign both boundary conditions and loads. The nodal configuration used in the code obeys a systematic approach allowing the supports and external loads to be easily defined. Each node within the discretized domain has three degrees of freedom in accordance with the displacements along with x-y-z directions [23]. The discretized domains are partitioned to multiple eight-noded cubic elements based on the volume of the design domain. The location of the nodes is specified using a Cartesian coordinate system. The cubic elements are composed of eight-nodes, which are arranged in a counter clock-wise manner.

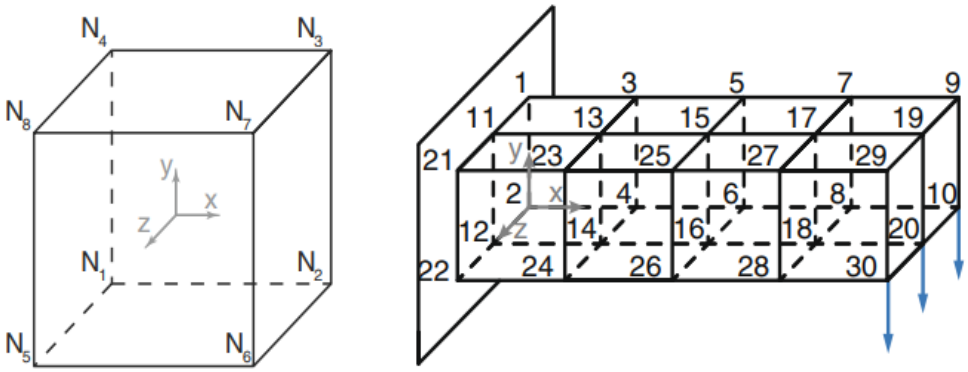

Figure 3.2 Left cubic element, right discretized domain [24].

A relationship between nodal elements is established throughout the optimization process. Since the nodes are related to each other using a mapping configuration, the identification of the nodal coordinates can be deduced from the assigned volume of the design domain ($nelx \times nely \times nelz$) and the coordinates of the node $N_1(x_1, y_1, z_1)$.

The coordinates of the remaining nodes are obtained using the following relationships:

Table 3.1 Relationships between nodes [25].

Node Number	Node coordinates	Node ID	Node Degree of Freedoms		
			x	y	z
N_1	(x_1, y_1, z_1)	$\text{NID}_1^{\dagger}$	$3*\text{NID}_1-2$	$3*\text{NID}_1-1$	$3*\text{NID}_1$
N_2	(x_1+1, y_1, z_1)	$\text{NID}_2=\text{NID}_1+(\text{nely}+1)$	$3*\text{NID}_2-2$	$3*\text{NID}_2-1$	$3*\text{NID}_2$
N_3	(x_1+1, y_1+1, z_1)	$\text{NID}_3=\text{NID}_1+\text{nely}$	$3*\text{NID}_3-2$	$3*\text{NID}_3-1$	$3*\text{NID}_3$
N_4	(x_1, y_1+1, z_1)	$\text{NID}_4=\text{NID}_1-1$	$3*\text{NID}_4-2$	$3*\text{NID}_4-1$	$3*\text{NID}_4$
N_5	(x_1, y_1, z_1+1)	$\text{NID}_5=\text{NID}_1+\text{NID}_z^{\ddagger}$	$3*\text{NID}_5-2$	$3*\text{NID}_5-1$	$3*\text{NID}_5$
N_6	(x_1+1, y_1, z_1+1)	$\text{NID}_6=\text{NID}_2+\text{NID}_z$	$3*\text{NID}_6-2$	$3*\text{NID}_6-1$	$3*\text{NID}_6$
N_7	(x_1+1, y_1+1, z_1+1)	$\text{NID}_7=\text{NID}_3+\text{NID}_z$	$3*\text{NID}_7-2$	$3*\text{NID}_7-1$	$3*\text{NID}_7$
N_8	(x_1, y_1+1, z_1+1)	$\text{NID}_8=\text{NID}_4+\text{NID}_z$	$3*\text{NID}_8-2$	$3*\text{NID}_8-1$	$3*\text{NID}_8$

$^{\dagger}\text{NID}_1 = z_1$*(nelx+1)*(nely+1)+$x_1$*(nely+1)+(nely+1 − y_1)

$^{\ddagger}\text{NID}_z$ = (nelx+1)*(nely+1)

From the previous table, it is apparent that all the node coordinates depend on N_1. The identification of a node depends on the boundary conditions and the load application within the design domain. In the optimization code, the node coordinates are arranged using a connectivity matrix **edofMat** throughout the following lines [26]:

```
nele = nelx*nely*nelz;
ndof = 3*(nelx+1)*(nely+1)*(nelz+1);
F = sparse(loaddof,1,-1,ndof,1);
U = zeros(ndof,1);
freedofs = setdiff(1:ndof,fixeddof);
KE = lk_H8(nu);
nodegrd = reshape(1:(nely+1)*(nelx+1),nely+1,nelx+1);
nodeids = reshape(nodegrd(1:end-1,1:end-1),nely*nelx,1);
nodeidz = 0:(nely+1)*(nelx+1):(nelz-1)*(nely+1)*(nelx+1);
nodeids = repmat(nodeids,size(nodeidz))+repmat(nodeidz,size(nodeids));
edofVec = 3*nodeids(:)+1;
edofMat = repmat(edofVec,1,24)+ ...
    repmat([0 1 2 3*nely + [3 4 5 0 1 2] -3 -2 -1 ...
    3*(nely+1)*(nelx+1)+[0 1 2 3*nely + [3 4 5 0 1 2] -3 -2 -1]],nele,1);
```

Figure 3.3 Arrangement of nodal coordinates [27].

nele: total number of elements.

nodegrd: comprise the node ID of the x-y plane (z=0) of the first grid nodes.

edofVec: consists of the ID nodes at each element.

The connectivity matrix **edofMat** of size **nele×24** comprises the node IDs of each element.

3.4 Boundary Conditions and External Loads

```
% USER-DEFINED SUPPORT FIXED DOFs
iif = [0 0 nelx nelx]; jf = [0 0 0 0]; kf = [0 nelz 0 nelz]; % Coordinates
fixednid = kf*(nelx+1)*(nely+1)+iif*(nely+1)+(nely+1-jf); % Node IDs
fixeddof = [3*fixednid(:); 3*fixednid(:)-1; 3*fixednid(:)-2]; % DOFs
```

Figure 3.4 Lines of fixed boundary conditions related to the MBB-beam configuration [28].

jf , kf : coordinate of the fixed nodes.

fixednid : node IDs.

fixeddof : location of the degrees of freedom.

```
% USER-DEFINED LOAD DOFs
il = nelx/2; jl = nely; kl = nelz/2;                    % Coordinates
loadnid = kl*(nelx+1)*(nely+1)+il*(nely+1)+(nely+1-jl); % Node IDs
loaddof = 3*loadnid(:) - 1;                             % DOFs
```

Figure 3.5 Lines of load degrees of freedom related to the MBB-beam configuration [29].

The chosen nodes of both boundary conditions and external loads are important during a topology optimization problem. The optimization code defines both active and passive elements that are essential in the process of density removal throughout the iterative SIMP algorithm. Generally, the defined boundary conditions are considered as passive elements meaning that the local densities near the boundary are kept untouched to preserve the main function of the initial geometry. Meanwhile, the active elements are included within the density removal process to reach an

optimal load-carrying path of the structure. A bad definition of the boundary condition of the topology optimization problem would alter the intended function of the initial design domain.

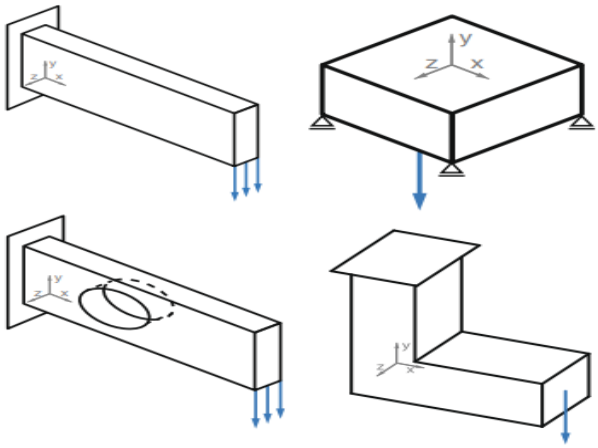

Figure 3.6 External loads within different design domains [30].

3.5 Results

The objective of this section is to examine the optimized model and describe the variation of compliance throughout the optimization process.

3.5.1 Case Study: Messerschmitt-Bölkow-Blohm (MBB-beam)

In this case study, an MBB-beam is subjected to structural optimization using four planar joints as boundary conditions, whereas the load is applied in the middle of the upper side of the structure. Using mechanical properties of stainless steel 316l: Young's modulus $E = 190\ GPa$ and Poisson's ratio $\nu = 0.265$.

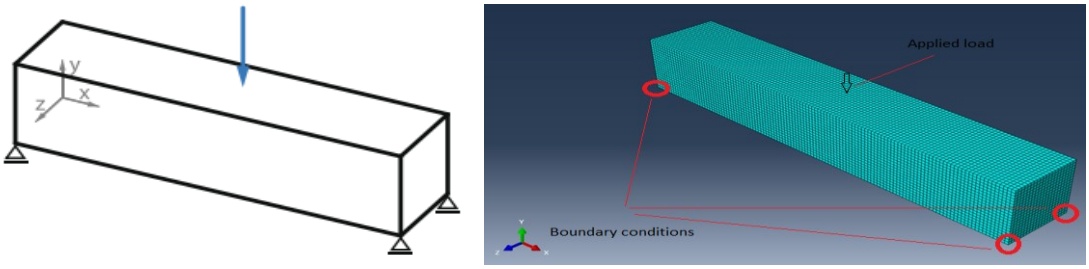

Figure 3.7 MBB-beam size $120 \times 20 \times 20$ [31].

$$6L \times L \times L$$
$$\text{mesh } 120 \times 20 \times 20$$
$$\bar{v} = 0.20,\ p = 3,\ R = 1.5$$

Figure 3.8 Value of parameters.

To solve the minimum compliance problem, the chosen volume fraction is 0.2 and the filter radius is 1.5 whereas the penalization factor is 3.

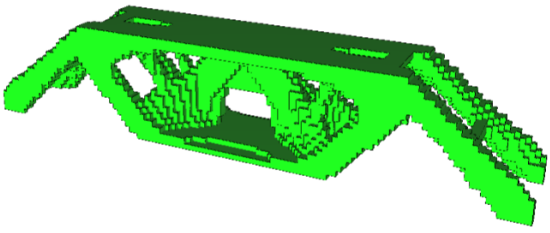

Figure 3.9 Final topology.

The optimization problem needed 30 iterations to reach the optimal solution.

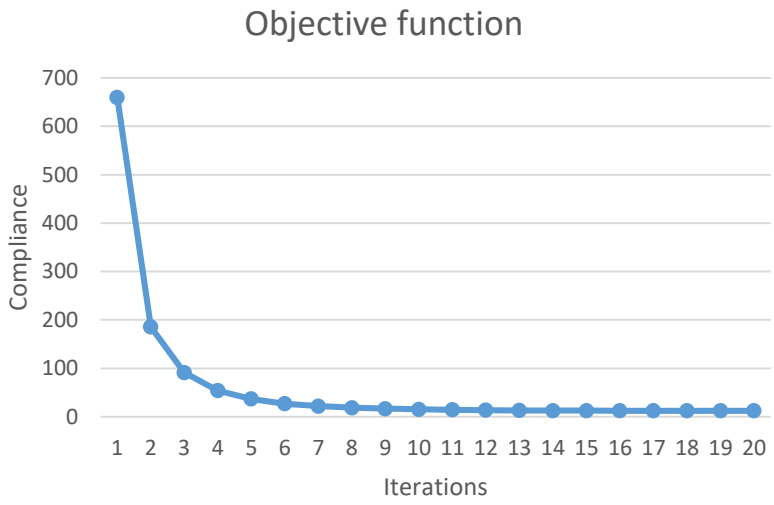

Figure 3.10 Variation of compliance.

3.5.2 Objective function per Iteration

Topological changes of the optimization iterations for MBB-Beam:

5, 10, 15, 20, 30, 40

Number of iterations: 5

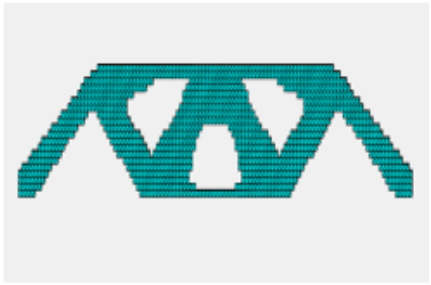

Number of iterations: 10

Number of iterations: 15

Number of iterations: 20

Number of iterations: 30

Number of iterations: 40

Figure 3.11 Topological behavior

The optimization problem needed 30 iterations to reach the optimal solution.

3.5.3 Influence of the Volume Fraction

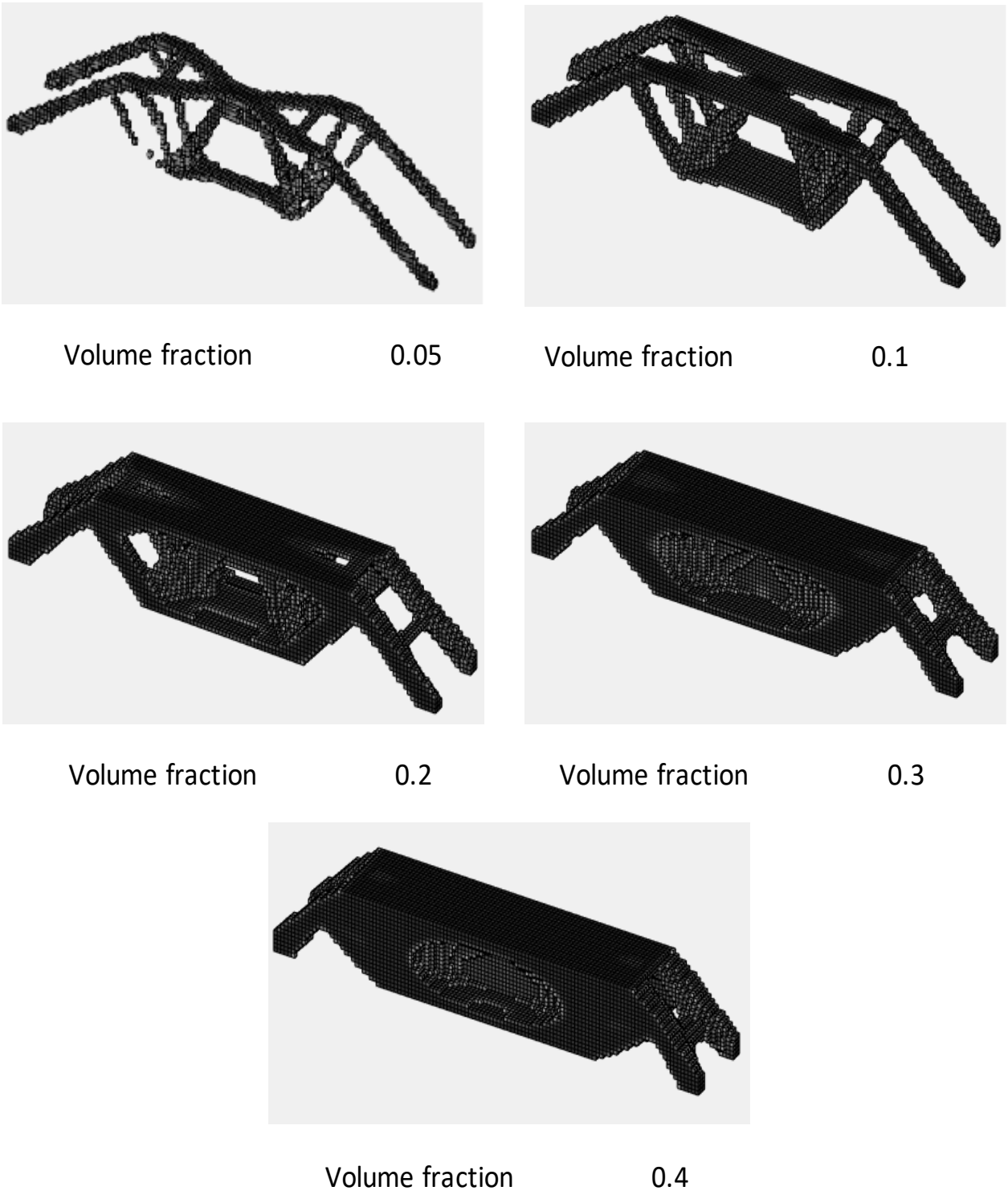

Figure 3.12 Effect of the volume on the final topology.

The volume fraction is an important factor in a topology optimization problem. Based on the final topologies of each volume fraction it is apparent that a big volume fraction results in a stiff structure. The material is exploited in full density.

3.5.4 Influence of the Filter Radius

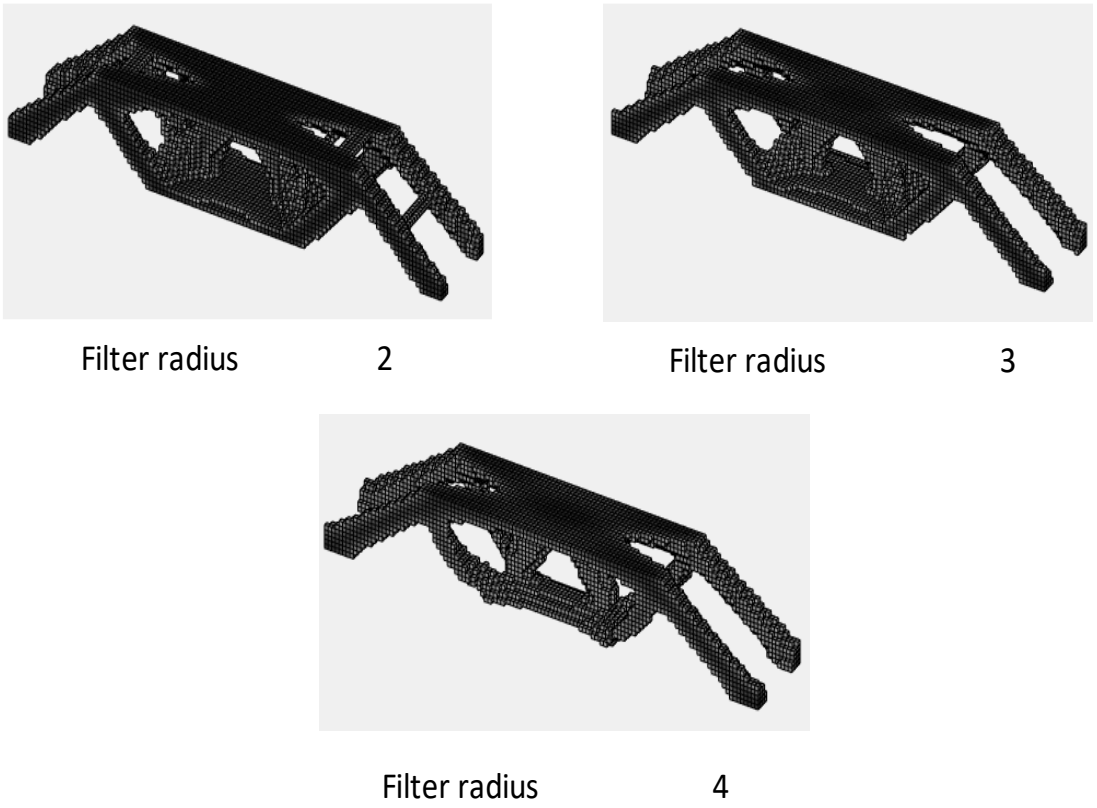

Figure 3.13 Effect of the filter radius on the final topology.

The main function of the filter radius is to eliminate the checkerboarding pattern resulting in a clear solid-void portioning of the elemental densities. Based on the obtained results in figure 3.16, the optimal filter radius in this case is 2. A filter radius higher than 2 affects the compliance of the

structures by eliminating most of the intermediate densities which are not completely dysfunctional.

3.5.5 Influence of the Gray-scale Penalty Factor

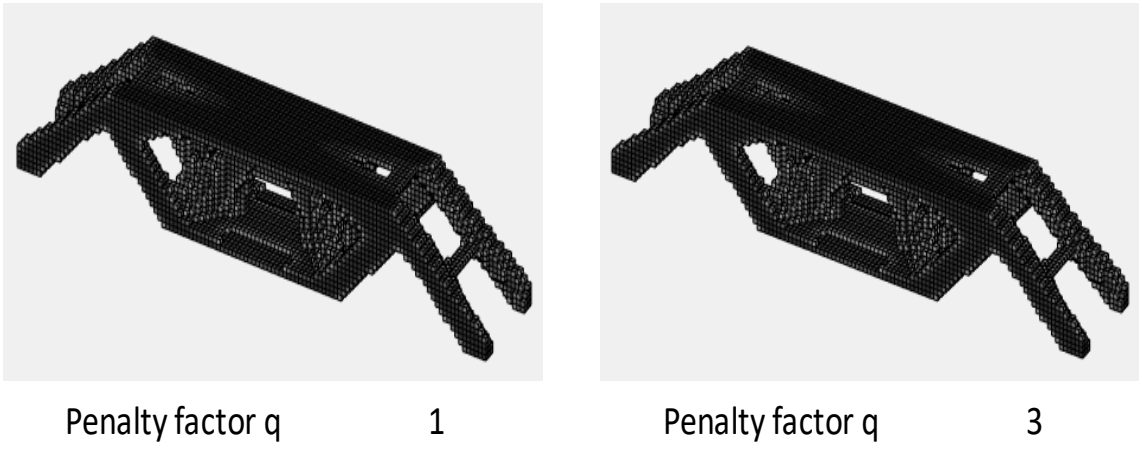

Figure 3.14 Effect of the gray-scale penalty factor.

The effect of the gray-scale factor is to lower the formation of intermediate densities to obtain a better compliance design as well as reach an optimum manufacturable topology without checkerboarding problems. A penalty factor equal to 1 diminishes the effect of the factor by producing more intermediate densities resulting in irrelevant solid-void regions.

CHAPTER IV

TAUBIN SMOOTHING METHOD AND POST-OPTIMIZATION OF MESH ERRORS

Geometric inconsistencies within meshes are difficult for 3D-printers. A denoising algorithm called Taubin smoothing method is used to filter high frequencies and smooth the optimized model. The smoothing method helps reduce the formation of residual stresses by eliminating angles prone to the overhang limit. In the meantime, the smoothing method succeeded in preserving both the shape and the geometric characteristics related to the topology optimization problem.

4.1 Mathematical Formulation

Taubin smoothing presented a new alternative instead of using the two-scale factors of opposite signs, which implements the negative factor of larger magnitude within the Laplacian smoothing approach.

Such implementation eliminates the high frequencies within the umbrella operator of the Laplacian smoothing while conserving the low frequencies. The rule that governs the Taubin technique is expressed as follow [32]:

$$P_{new} \rightarrow (1 - \mu\mathcal{U})(1 + \lambda\mathcal{U})P_{old} \tag{4.1}$$

$$= P_{old} - (\mu - \lambda)\mathcal{U}(P_{old}) - \mu\lambda\mathcal{U}^2(P_{old}),$$

Where $\mathcal{U}^2$ is the squared umbrella operator:

$$\mathcal{U}^2(P) = \frac{1}{\sum_i w_i}\sum_i w_i\mathcal{U}(Q_i) - \mathcal{U}(P) \tag{4.2}$$

According to Taubin, the best smoothing occurs when $\mathcal{U} = \mathcal{U}_0$ or$\mathcal{U} = \mathcal{U}_1$. The filtering scheme used by the method provides good performance results.

4.2 Mesh Smoothing of the Optimized Model

After achieving the final optimized form of the MBB beam problem, we import the STL file of the optimized part in Mesh LAB software. Both operators μ and λ are defined to obtain an optimal mesh smoothing without shrinkage of the optimized model. The following smoothing method preserved the shape and the geometric characteristics related to the boundary condtions implemented throughout the topology optimization problem. Moreover, the Taubin technique provided a smooth CAD representation of the optimized model by filtering geometric profiles prone to the overhang limit. The smoothing technique enabled an optimal additive manufacturing of the parts by reducing the formation of residual stresses within the structure.

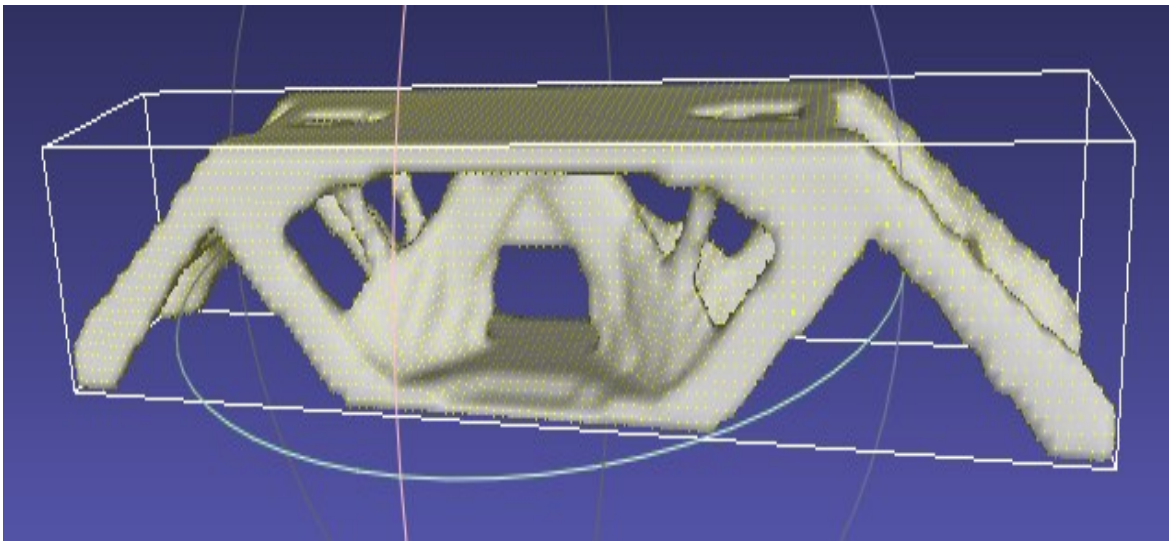

Figure 4.1 Smoothed mesh of the optimized model.

4.3 Post-optimization of Mesh Errors

After getting the final STL file of the optimized beam through MATLAB, we found multiple deficiencies in the design such as invalid faces and gaps. At this phase the changes must be done manually using two approaches either 'tracing' the optimization result or using a form of recognition feature [33]. This both techniques are not efficient in terms of geometry preservation. The main purpose of this section is to describe the common errors within the boundary representation of CAD models such as surface gaps, non-manifold vertices, degenerate facets and intersecting facets. These errors commonly exist in solid models due to imprecise arithmetic resolutions of geometries and programming inconsistencies. These types of errors obstruct critical analyses of solid models such as finite element analysis and rapid prototyping. The repair process used throughout the project is the import diagnostics feature provided by SOLIDWORKS manual.

Furthermore, the import diagnostics feature reveals surface issues using the following process [34]:

- Running checks on overlapping surfaces.
- Replace unsimplified surfaces with equivalent analytical surfaces to improve the performance of the CAD model.

The import diagnostics feature repairs the geometric errors using the following steps:

- Redesign omitted surfaces based on the surrounding geometry of the model.
- Omit irrelevant portions within faces.
- The gap repair algorithm is used to fill the resulting voids due to removed faces.

In addition, the import diagnostics eliminates the gaps between adjacent faces by doing one or more of the following:

- Unify two close but nonintersecting edges.
- Add surfaces to fill the existing gap.
- Eliminate gaps by extending two adjacent faces into each other.

Additional functionality:

- Transform unsimplifed surfaces into analytic surfaces.
- Use the knit feature to merge repaired faces into the surface body.
- Transform the body into a solid if the surface body is closed.

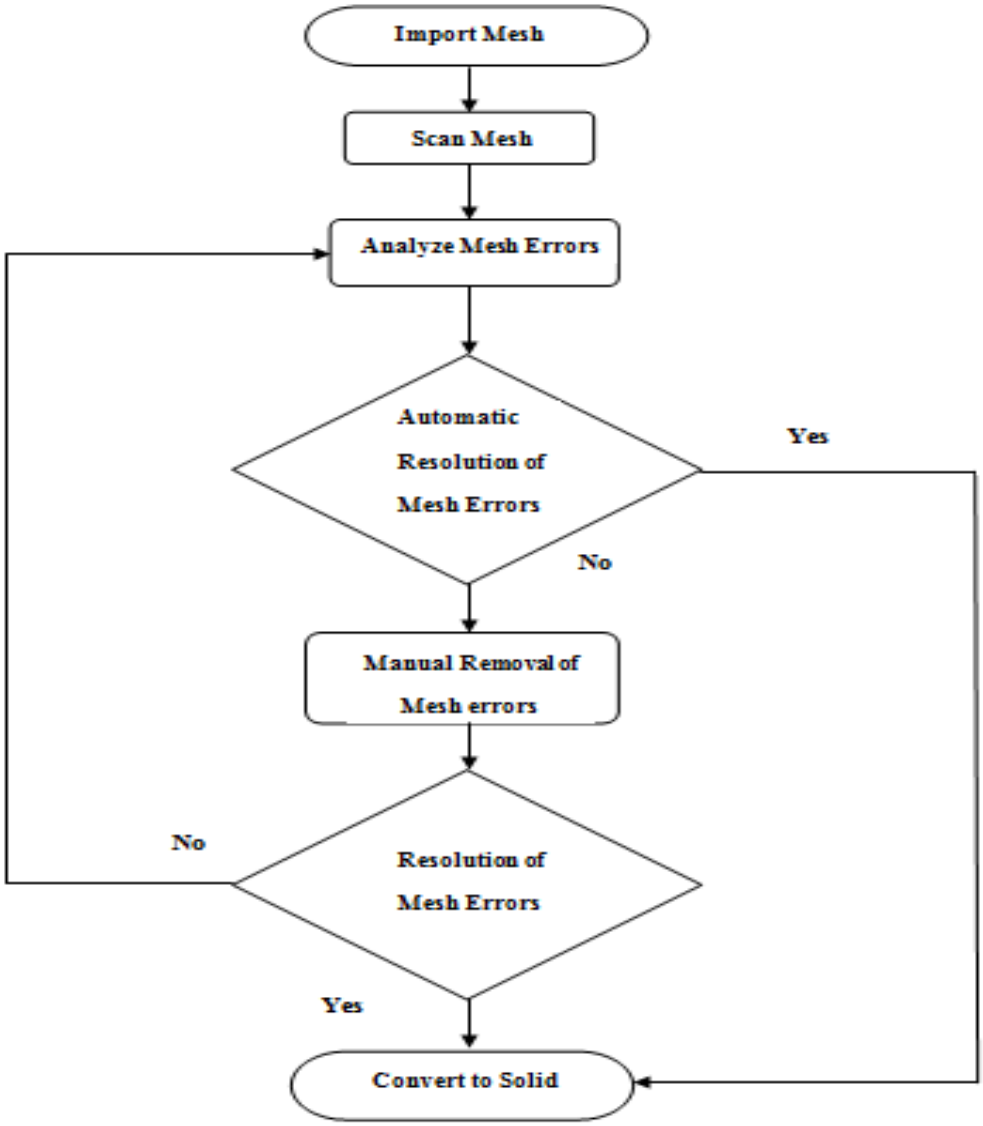

Figure 4.2 Steps of post-optimization steps.

4.3.1 Mesh Errors

After getting the numerical results via optimization codes in STL format, comes the part where the resulted meshes must be investigated in order to correct the problems that could occur when generating the results through MATLAB.

The most common problems that could be encountered in this case are [35]:

1. Surface gaps or misplaced facets.
2. Non-manifold vertices.
3. Degenerate facets.
4. Intersecting facets.

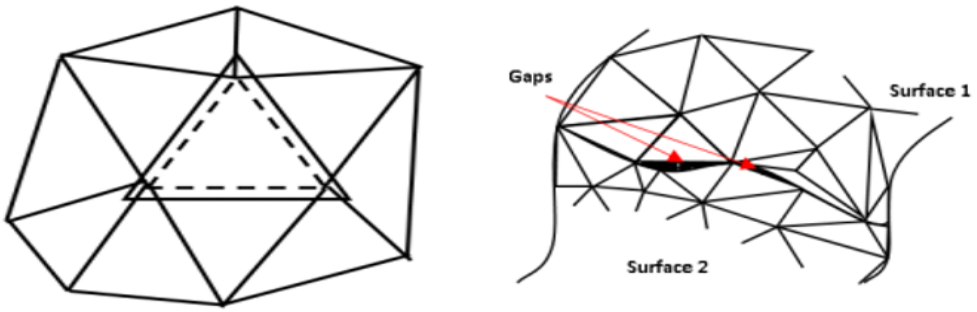

Figure 4.3 Illustration of gaps within meshes [36].

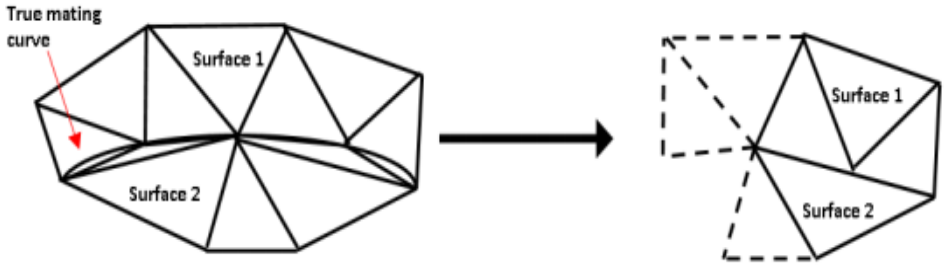

Figure 4.4 Degenerated facets [37].

During the tessellation of surfaces with large curvature, a lot of errors can occur in the overlapping of surfaces, engendering gaps within the edges of the part [38]. For a manifold edge of being valid, it has to have one edge shared by two facets only. In fact, a non-manifold edge is

generally shared by four different facets. In order to fix the non-manifold edge problematic, each facet has to have one neighbor facet along each edge. Types of non-manifold errors:

- Non-manifold edge.
- Non-manifold point.
- Non-manifold face.

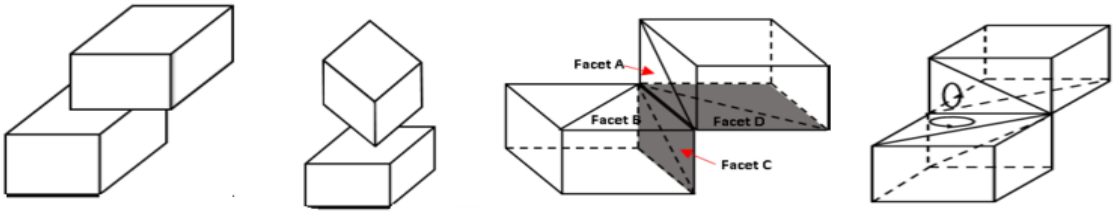

Figure 4.5 Types of non-manifold errors [39].

4.3.2 Mesh Repair

After importing the STL file on SOLIDWORKS, the import diagnostics feature is launched to run an analysis on the mesh. The depicted errors were corrected using both the import diagnostics feature and a manual approach on SOLIDWORKS. The existing errors are the following:

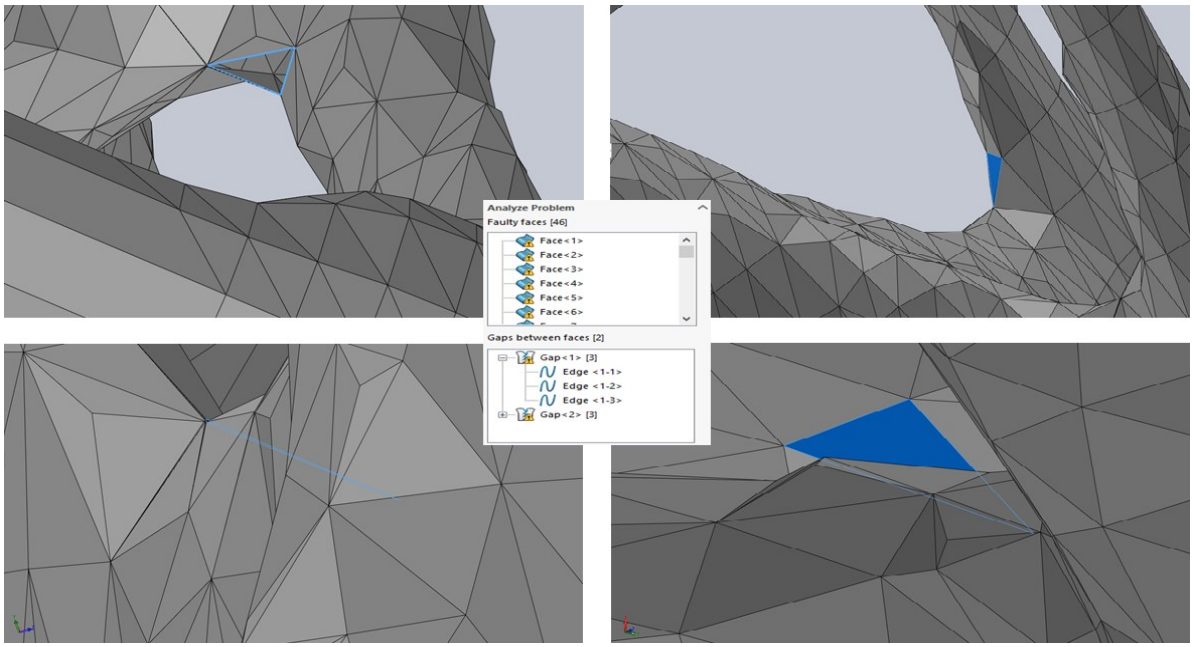

Figure 4.6 Errors within the mesh of the optimized model.

Based on the import diagnostics scan, the mesh had several intersecting surfaces as well as internal surface gaps especially at the center of the model. The denoising approach of the umbrella operator of Taubin smoothing converted the surface of the optimized model to a smooth representation allowing the triangular faces of the mesh to have approximately the same level of curvature, which made the knitting feature and the gap filling easier.

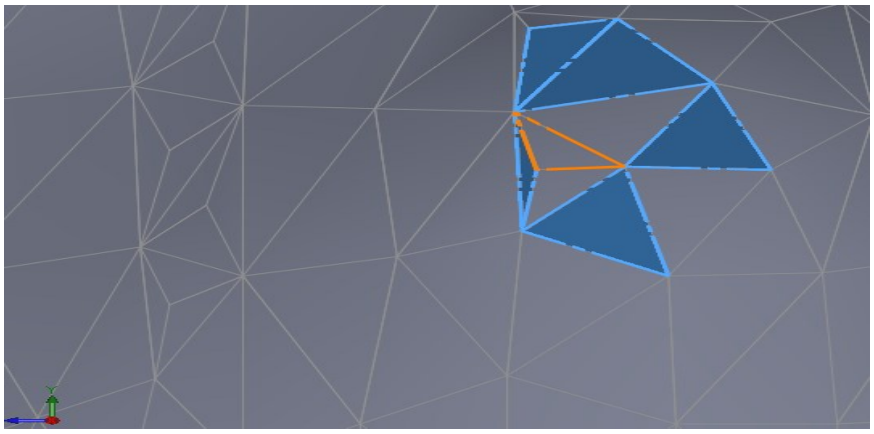

Figure 4.7 Example of connected pattern of intersecting faces.

Figure 4.8 Example of a surface gap.

CHAPTER V

FINITE ELEMENT ANALYSIS

In the following chapter, a numerical model is set to simulate the bending mechanism of the CAD model. Throughout the analysis, a three-point bending test was modeled using the same boundary conditions and external loads observed during the experimental tests. The mechanical properties implemented in the simulation are based on previous researches made on stainless steel 316l since the value of Young's modulus depends on the build orientation as well as the induced residual stresses through the selective laser melting process. The reason behind adopting the findings of the specific research is to obtain results capable of predicting the behavior of stainless steel 316l accurately. The built parts have a different microstructure compared to the CAD model; they exhibit an anisotropic behavior, which is not the case for the numerical model. The software used throughout this section is ABAQUS.

5.1 CAD Model

The model was imported in ABAQUS FEA software to investigate the deformations of the structure; the analysis simulates the three-point bending test that was similar to the boundary conditions used during the experiment. The supporting feet were added in order to fit the structure throughout the 3 points bending test apparatus.

Figure 5.1 Designed model.

5.2 Material Properties

Based on the mechanical properties in [40], we have the values of Young's Modulus in three different build orientations. The reason behind choosing the young's modulus from the table; because the measurements of the parameter took into considerations the anisotropic behavior of additively manufactured stainless steel 316l as well as the effects of both build orientation and residual stresses induced throughout the printing process.

This approach allows us to simulate a more realistic young's modulus in an anisotropic point of view to depict the flexural behavior accurately. From the data of (Merkt et al., 2015), we choose the minimum value of Young's modulus which is 160 GPa in order to evaluate the lowest case scenario possible for our printed models. Moreover, the chosen value of Young's modulus is 45°, which is the same build orientation used throughout the printing process of the models. The material properties assigned to the model are chosen based on previous researches done on the behavior of stainless steel 316l under the effect of selective laser melting technique such as the print orientation, heat treatment, and residual stresses.

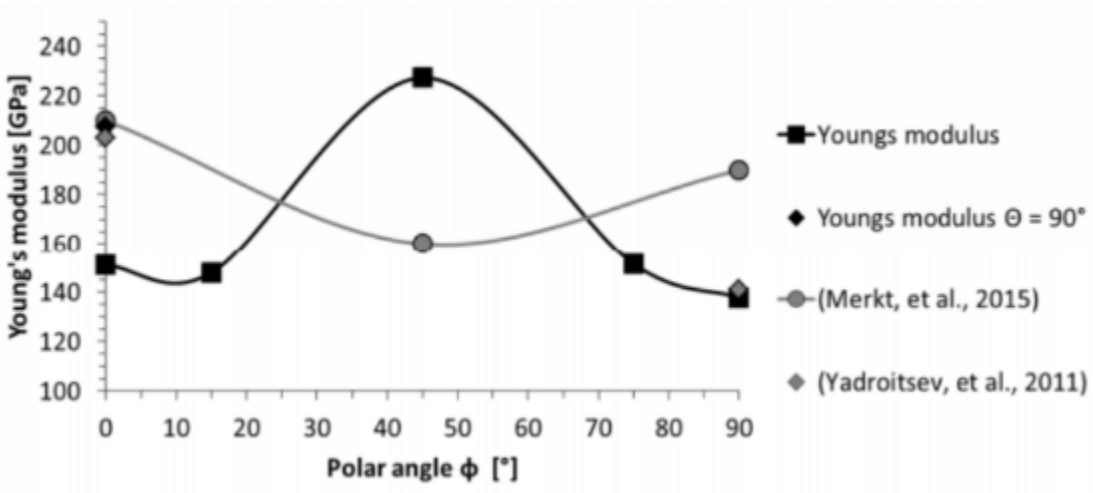

Figure 5.2 Variation of Young's Modulus with respect to the build orientation [41].

The graphs below illustrate the variation of young's modulus under different printing angles, the choice of Young's modulus is based on the results of (Merkt, et al., 2015).

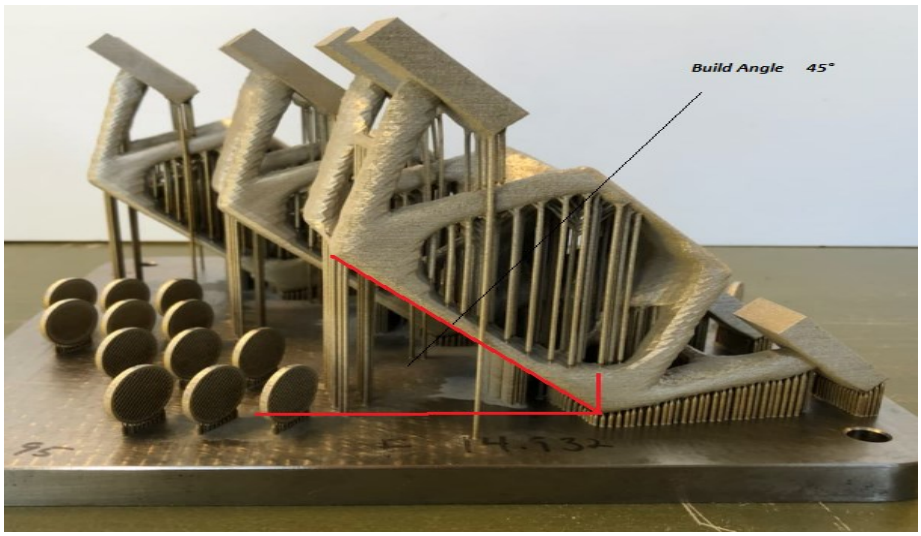

Figure 5.3 Build orientation of the printed models.

The finite element model uses a linear isotropic material behavior of the CAD model assuming perfect bonding between the layers.

5.3 Boundary Conditions

A finite element analysis was conducted on the CAD model of the printed beams in order to examine the flexural behavior of the parts and set a comparative analysis between the numerical and the experimental results. The numerical model was simulated using ABAQUS.

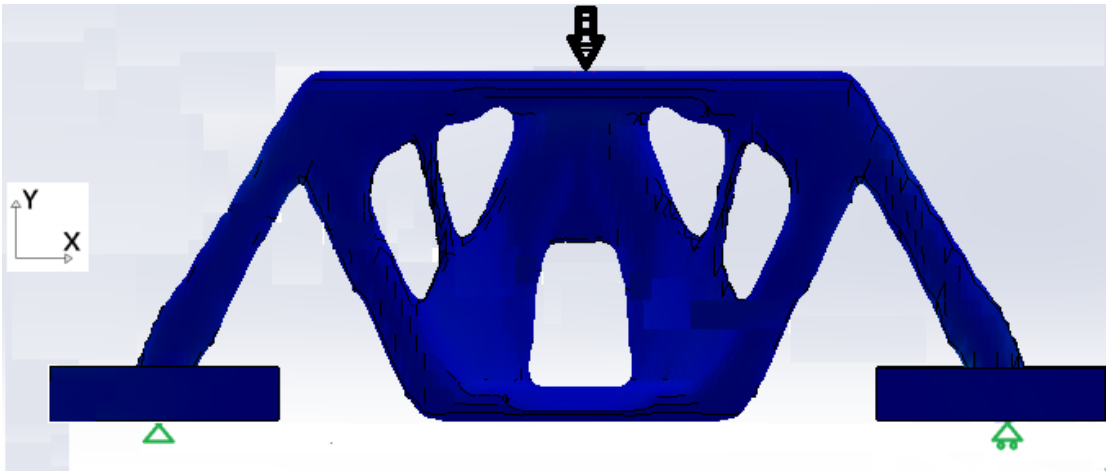

Figure 5.4 Boundary conditions and external loads of the model.

The mechanical behavior at each boundary condition (interaction with supports of the simulation) is explained as follow:

1. For the left-hand side: X translation allowed, rotation along Y-axis is not permitted UY=0, but rotations UZ and UX are preserved.
2. For the right-hand side: RY=0 along the line of contact and the rotation is permitted along the Z-axis and X-axis whereas UY=0. Translation allowed in the X-axis.
3. Displacement at the upper surface of the model.

In order to obtain an accurate numerical model of the three-point bending test, the boundary conditions were applied in accordance to the observed behavior of the specimens throughout the experiment; this approach enabled us to model the flexural bending test and get satisfying results compared to the experiment.

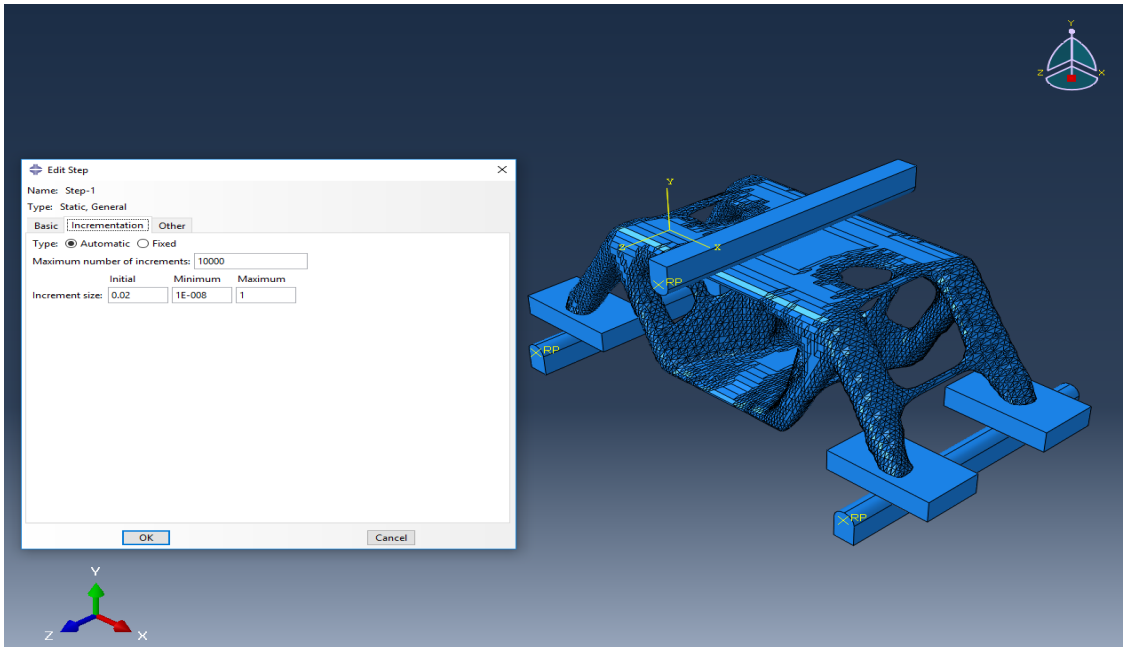

Figure 5.5 Step static-general.

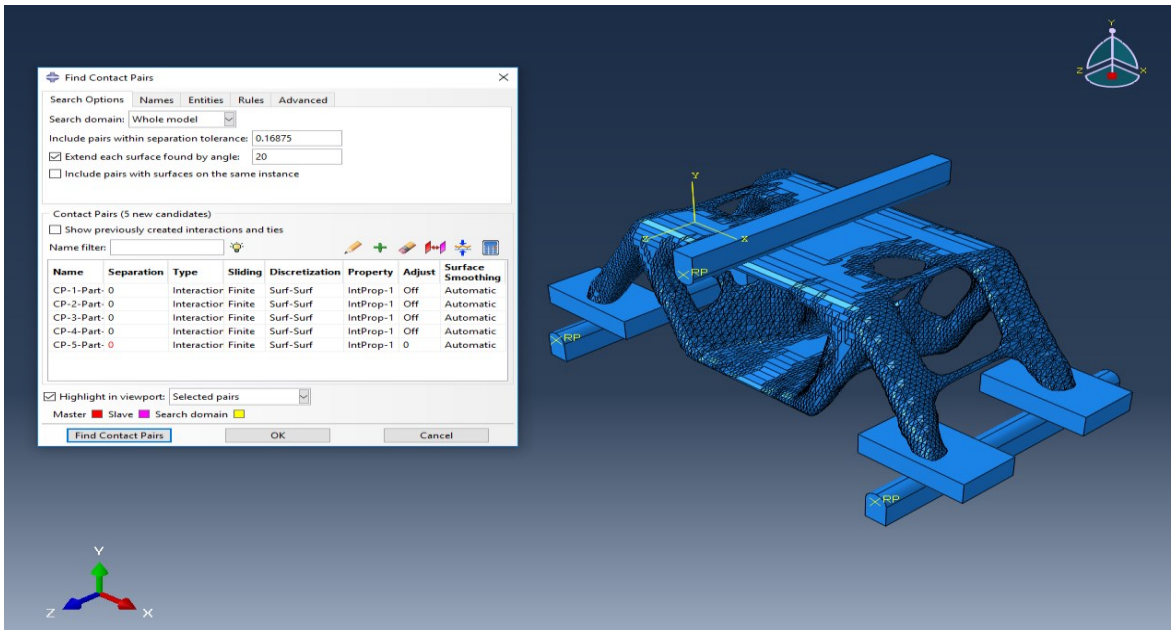

Figure 5.6 Contact interactions.

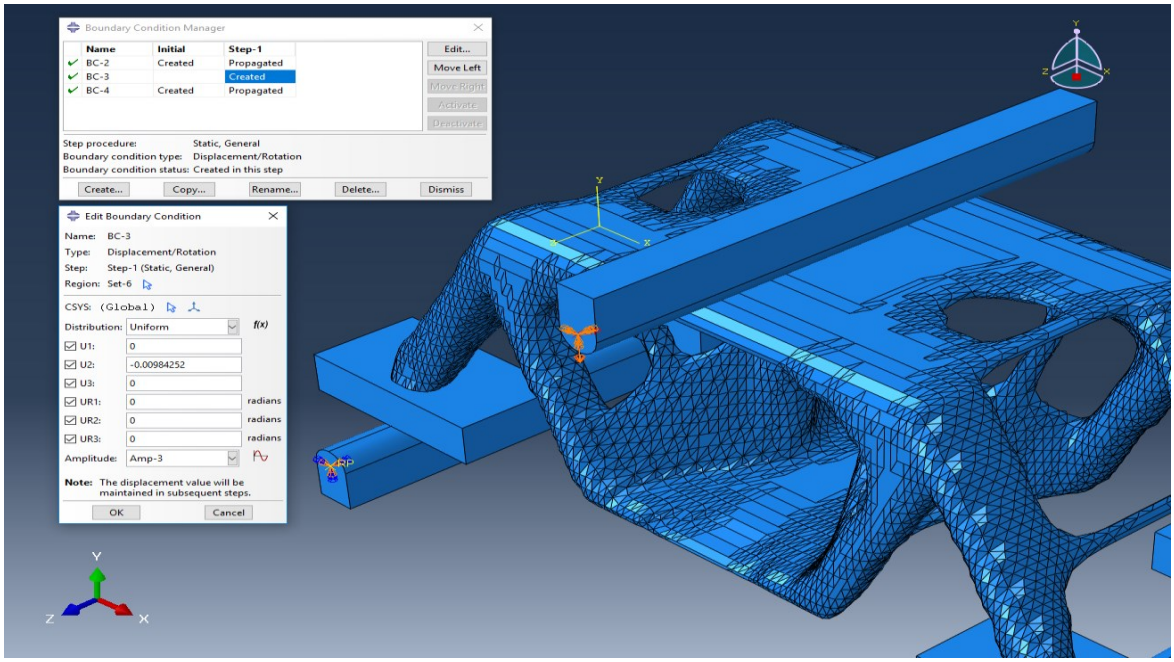

Figure 5.7 Displacement boundary condition.

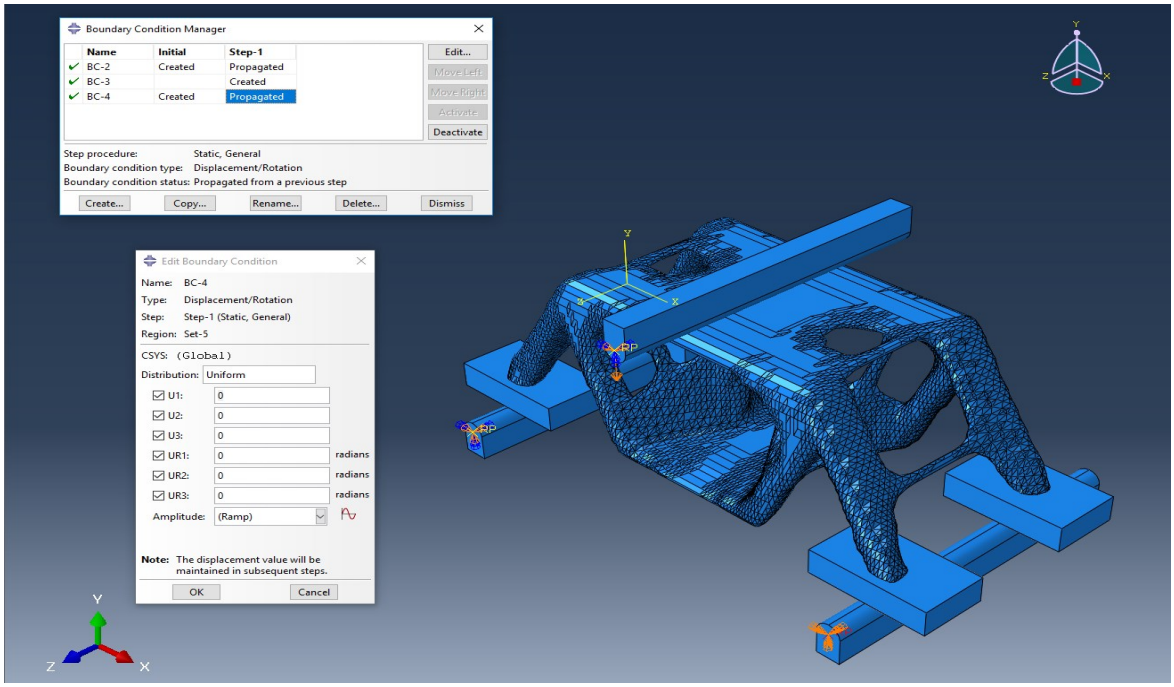

Figure 5.8 Supports boundary condition.

5.4 Mesh Generation

A curvature-based method is used to mesh the curved regions of the model. It determines the radius of curvature of each region in order to set a mesh that fits the geometric inclinations of the model. If sharp corners are in the load path, they are susceptible to high-stress concentrations. Based on this fact, the curvature-based technique generates tight meshes in these regions to provide accurate stress results. In addition, the curvature-based method is able to generate more mesh elements in case of meshing sophisticated models, which is not always possible for the standard method. Moreover, the curvature-based mesh performs well using a multi-core meshing [42].

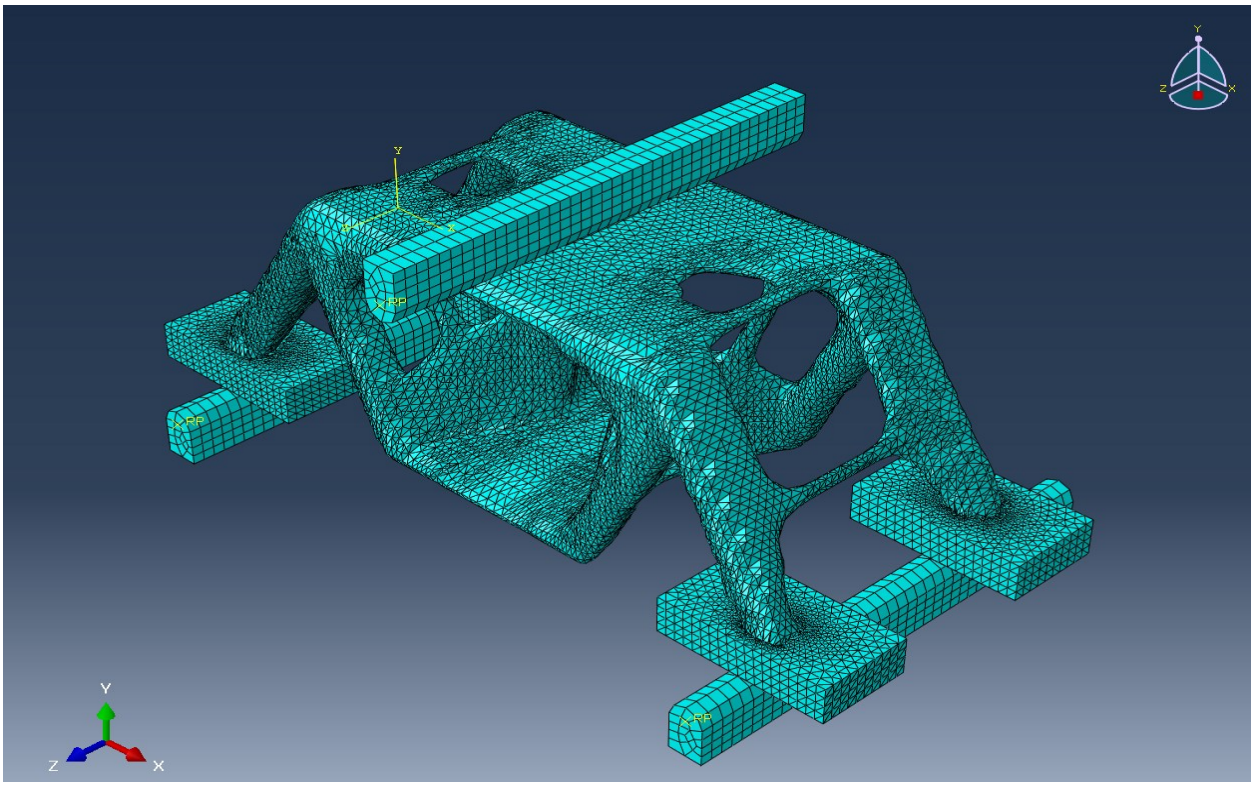

Figure 5.9 Meshed model.

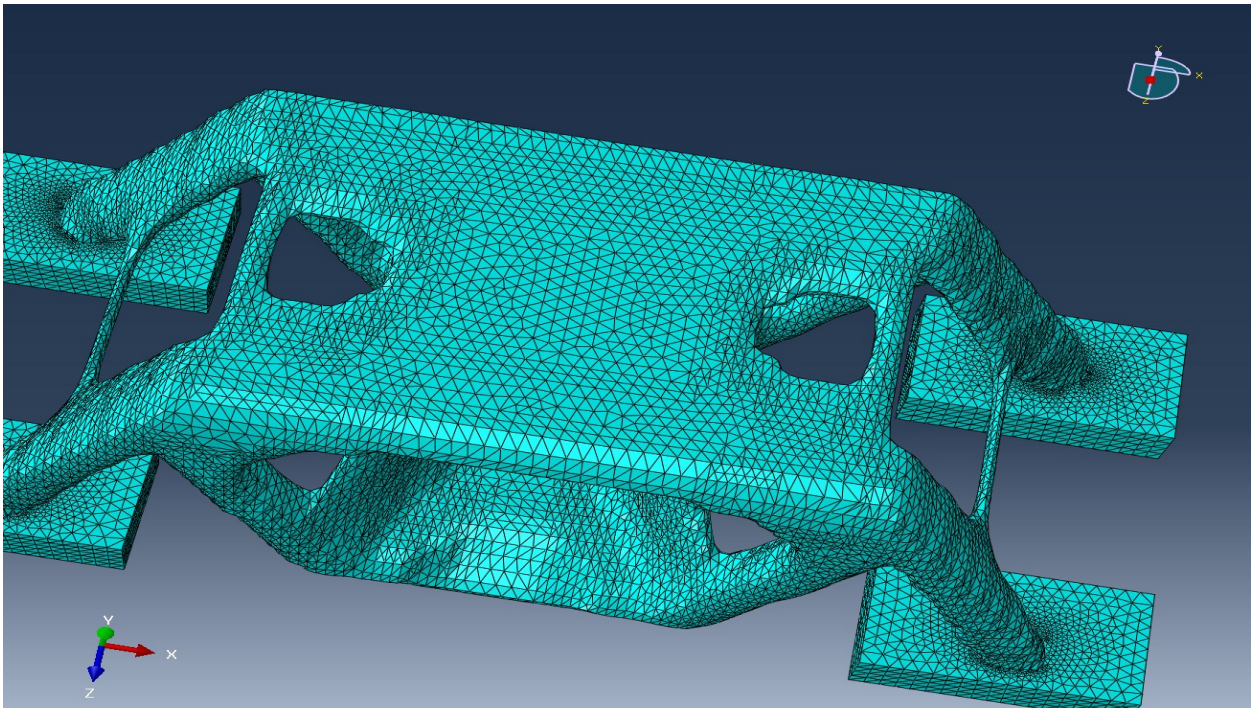

Figure 5.10 Region of displacement.

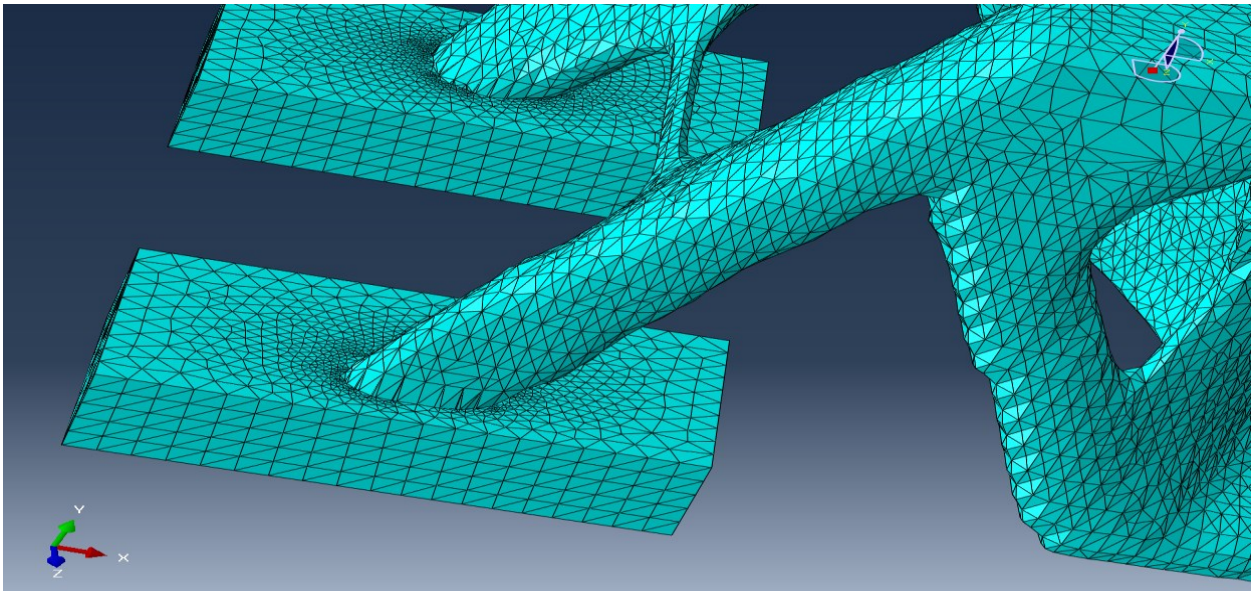

Figure 5.11 Side-view of the supporting feet.

Based on the mesh of the model, most of the regions have tight mesh, and that is due to the topology optimization problem since the main objective of structural optimization is to find an optimal load-carrying path, which is associated with the highest stress distribution.

5.5 Results of the Numerical Model

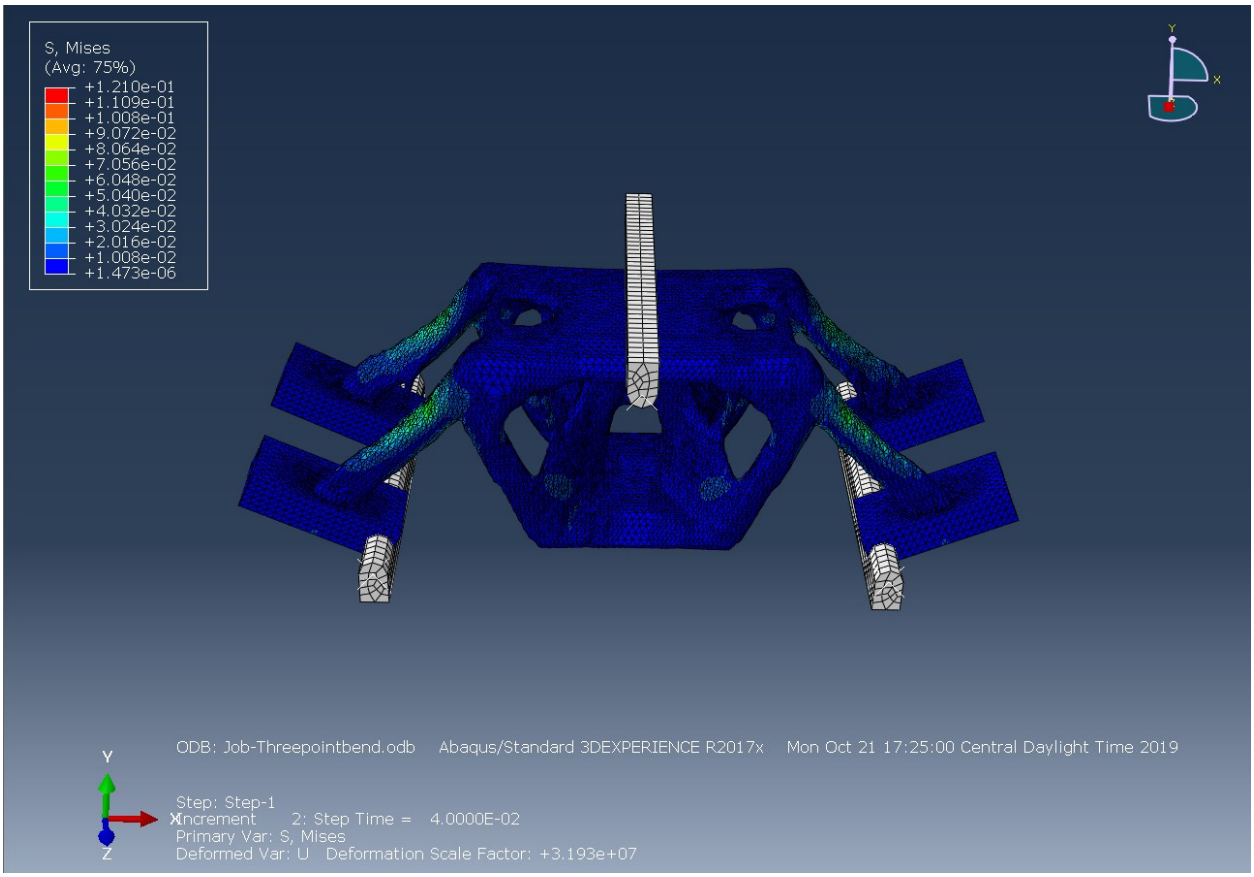

Figure 5.12 Von Mises stress distribution.

Based on the results of the Von Mises stress distribution, the feet of the model are exposed to higher stress concentrations compared to the remaining regions. The observed flexural behavior throughout the numerical simulation exhibited similar deformation as the built model during the experimental test.

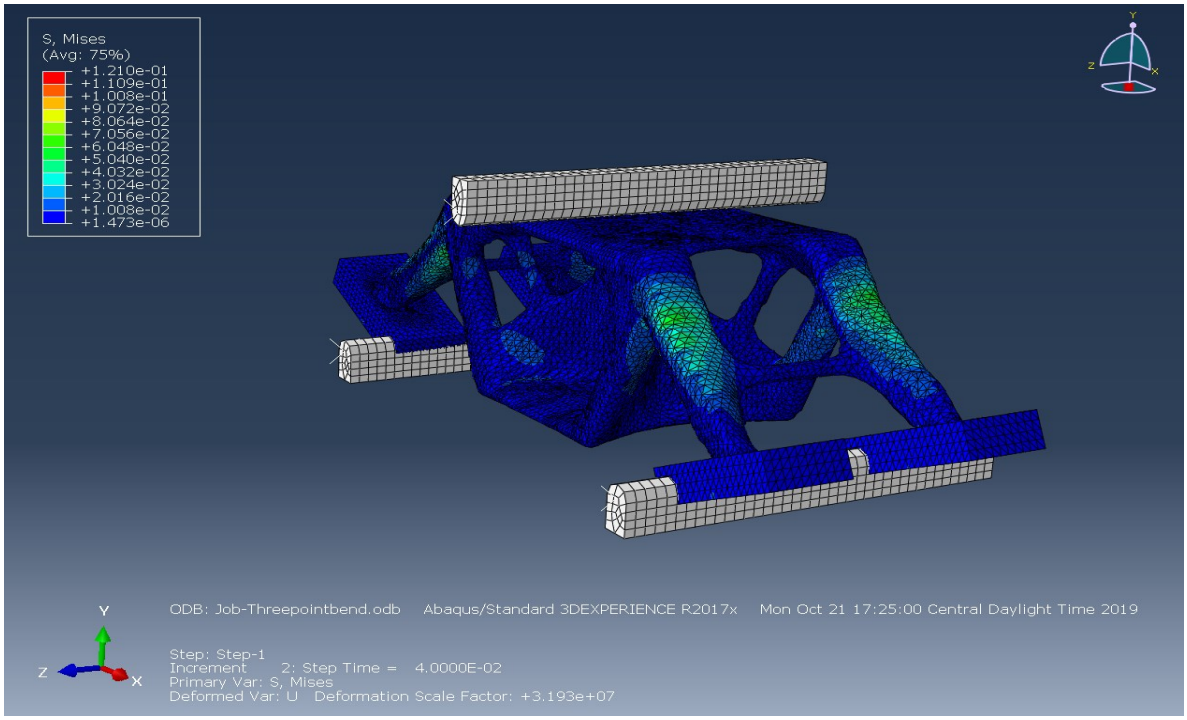

Figure 5.13 Deformation form.

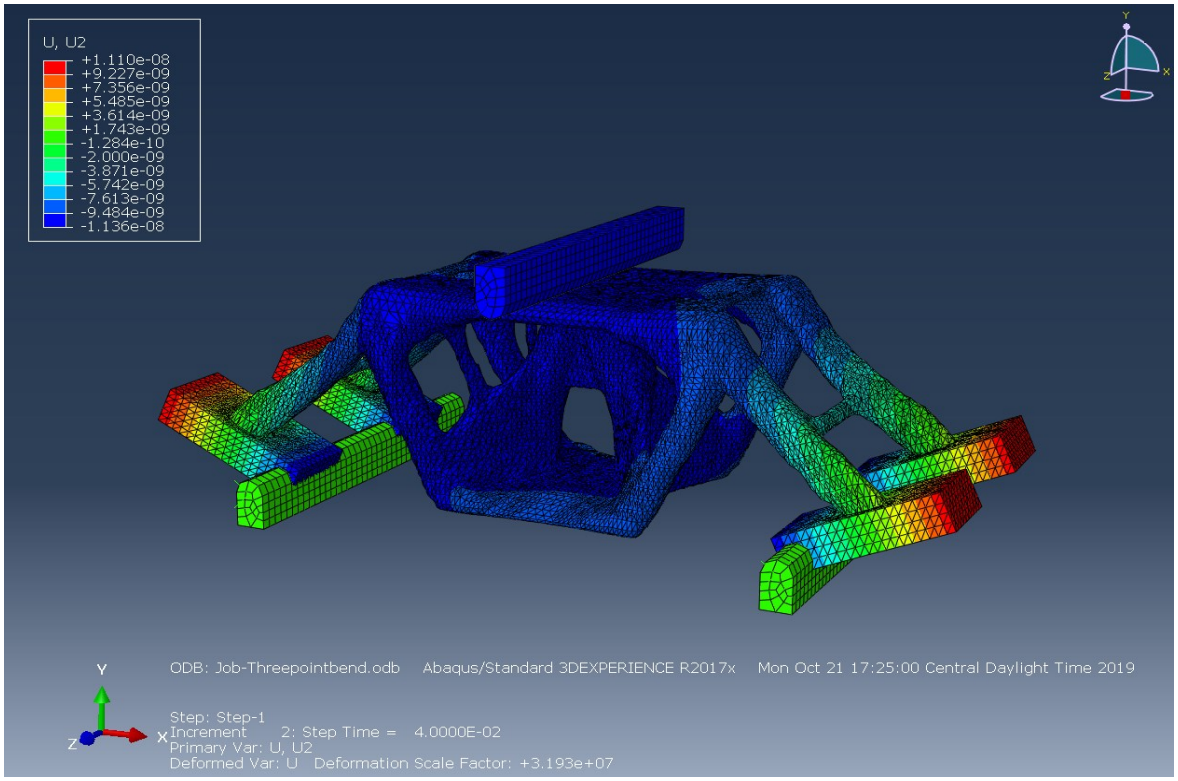

Figure 5.14 Displacement results.

CHAPTER VI

ADDITIVE MANUFACTURING

The term rapid prototyping signifies the production of 3D Models using 3D printing process; models are designed through 3D CAD software. Additive manufacturing uses 3D-printing process in order to get the desired product. This printing method superposes material in form of cross-sections using the layer-by-layer technique. In fact, printing thinner layers provides an accurate result compared to the designed model on the CAD software. Moreover, the layer-by-layer technique helps minimize both the printing duration and cost, in the meantime it could operate using multiple metallic and plastic materials.

Furthermore, additive manufacturing operates using multiple technologies that differ from each other in terms of performance, duration and cost. The most known technologies are stereolithography (SLA) and fused deposit modeling (FDM). Before the development of the layer-by-layer technique, the fabrication of models consisted of using a process called subtractive manufacturing which produces models by discarding materials from existing metallic specimens to obtain the desired shapes [43].

In fact, additive manufacturing process reduces the possibility of additional tooling and controls the production accurately compared to the conventional technique. Although, additive manufacturing has ameliorated tremendously the manufacturing process, still it suffers from multiple limitations regarding the design such as the chamber's dimension of the machine which constraints the dimensions of the desired design. In addition to that both surface finish and

dimensional precision are less accurate than the results obtained using the conventional technique [44]. Additive manufacturing process can operate using multiple technologies such as Stereolithography (SLA), Direct Metal Laser Sintering (DMLS), Selective Laser Sintering (SLS) and Selective Laser Melting (SLM). Each technology has a different method to achieve the desired printings, these techniques affects majorly both the performance and cost of the manufacturing process. For instance, Stereolithography uses a laser beam that scans over specific surfaces that are constituted of photopolymers; the beam follows a predefined pattern that assures the formation of the desired models. Moreover, Selective Laser Melting uses a laser beam to melt metals by fusing thin layers of metallic powders. Both Direct Metal Laser Sintering and Selective Laser Sintering use the sintering technique as in Selective Laser Melting, but they differ regarding the melting degree of the metal. The building process of additive manufacturing depends on multiple parameters. Most of these factors, affect the mechanical properties and the quality of the printed parts. Since we are interested in testing additively manufactured parts, it is essential to illustrate the impact of these parameters on the microstructure and the material of the manufactured structures.

Figure 6.1 Steps of 3D printing [45].

6.1 Additive manufacturing constraints

The major concern of topology optimization is to obtain an optimal material distribution within a predefined design domain. In fact, the material distribution result that is obtained through topology optimization is unconstrained by the domain connectivity which allows it to produce innovative designs. Nowadays, structures are more complex than before, they require accurate manufacturing approaches. Furthermore, classical manufacturing processes are overpriced and time consuming whereas additive manufacturing provides higher performance within a predefined time slot and it is less expensive. Moreover, coupling topology optimization with additive manufacturing seems to be efficient. Indeed, additive manufacturing provides a tremendous flexibility towards designing complex structures. Additive manufacturing is having two types of constraints which are classified as directional and non-directional regarding the nature of the design. For instance, the directional constraint is related to the printing direction of designed structure. Whereas, the non-directional constraint concerns both enclosed voids and minimum feature size [46]. Examples of directional constraints such as the overhang support and the layer induced anisotropy.

6.1.1 Directional Constraints

Since the printing direction is a crucial component that affects majorly the quality of designs, it is vital to ameliorate it. Moreover, there are multiple directional constraints that should be taken into consideration while improving the print direction such as layer induced anisotropy, thermal warping and overhang support. Furthermore, these constraints should be improved to enhance the orientation which is necessary to the print direction [47]. As a result of the thermal activity within the additive manufacturing process; residual stresses are induced due to local melting and nonuniform cooling of the manufactured design. Indeed, support structures are

implemented because of residual stresses and heat dissipation; in order to reduce these effects through the manufacturing process. Moreover, new methods were introduced to anticipate residual stresses in the designed parts [48]. Based on the layer induced anisotropy constraint some additive manufacturing methods proved that the in-plane print direction is more efficient than the print direction. In 2014, a new method was proposed that adjusts the theoretical model of optimization for additive manufacturing related to the overhang problem. The idea behind this method is to partition the inclination angle to three regions such as: robust zone ($40^{\circ} \leq \theta$), compromised zone ($40^{\circ} \leq \theta \leq 30^{\circ}$) and failed zone($30^{\circ} > \theta$). The obtained results showed that the support material was not used during the manufacturing process [49]. In 2017, a new method was presented that can be incorporated in conventional density-based topology optimization. The mesh has elements that are associated with a blue print-density; the elements that are sufficiently supported get printed [50]. The presented method focalizes on both SLM and EBM technologies. In case of a two-dimensional design problem an element within the design domain is supported via three elements underneath it.

6.1.2 Non-directional constraints

Some additive manufacturing technologies encounter the enclosed voids problematic while in process. For instance, during the SLM printing process the metallic powder stuck inside the voids of structures. In case of the fused deposition modeling, it is necessary to employ support structures within the designed part. These support structures are eliminated from the part after the achievement of the manufacturing process. In 2015, a method called virtual temperature method was introduced as a solution to the enclosed voids problem. The main idea behind this method is to fill the voids within structures using a virtual heating material characterized by high heat conductivity. Meanwhile, the solid regions are filled with a low heat conductivity material [51].

This approach enables the possibility of integrating the temperature constraint in topology optimization. Moreover, a new method called virtual scalar field method proposed that the temperature could be a scalar field in topology optimization [52]. In 2003, a scheme was introduced in order to integrate the minimum length scale feature within topology optimization [53]. Moreover, a newly proposed method demonstrates the possibility of attaining the minimum length scale by implementing geometric constraints within a filtering-threshold scheme of topology optimization; this concept implements both a density filter and a projection scheme [54].

6.2 Manufacturing Materials

Throughout the additive manufacturing there are multiple materials that can be used during the printing process such as metals, polymers and ceramics. These materials are categorized as follow:

Table 6.2 Types of materials used in the additive manufacturing process [55].

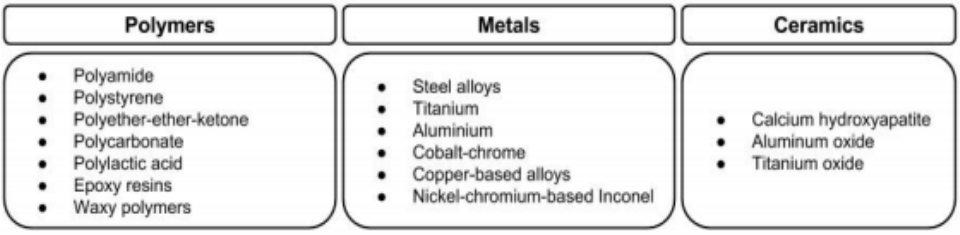

These materials operate on most commercial additive manufacturing machines. Each technology has a specific preference in terms of quality and cost.

Table 6.3 Mechanical properties of stainless steel 316l-0407 [56]

	As Built
Upper tensile strength (UTS) *(See note 2)*	
Horizontal direction (XY)	676 MPa ±2 MPa
Vertical direction (Z)	624 MPa ±17 MPa
Yield strength *(see note 2)*	
Horizontal direction (XY)	547 MPa ±3 MPa
Vertical direction (Z)	494 MPa ±14 MPa
Elongation at break *(see note 2)*	
Horizontal direction (XY)	43% ±2%
Vertical direction (Z)	35% ±8%
Modulus of elasticity *(see note 2)*	
Horizontal direction (XY)	197 GPa ±4 GPa
Vertical direction (Z)	190 GPa ±10 GPa
Hardness (Vickers) *(see note 3)*	
Horizontal direction (XY)	198 HV0.5 ±8 HV0.5
Vertical direction (Z)	208 HV0.5 ±6 HV0.5
Surface roughness (R_a) *(see note 4)*	
Horizontal direction (XY)	4 µm to 6 µm
Vertical direction (Z)	4 µm to 6 µm

6.3 Manufacturing Process

The additive manufacturing process is composed of eight steps:

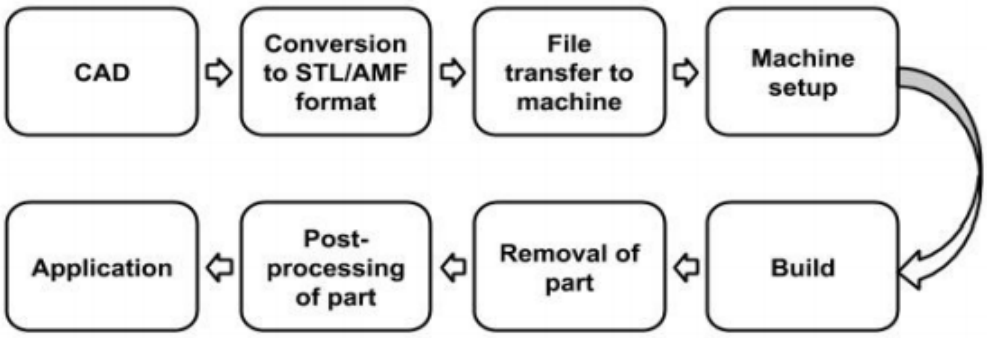

Figure 6.2 Steps of the additive manufacturing process [57].

6.4 Printed Models

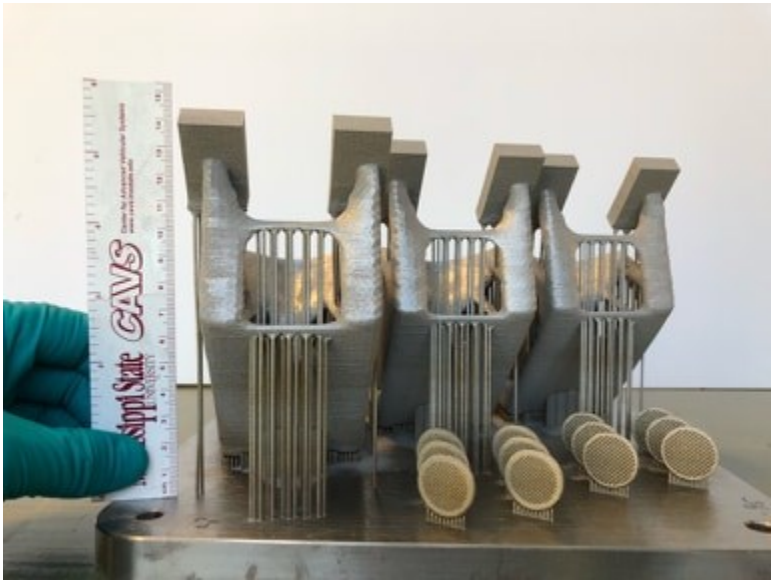

Figure 6.3 Front view of the printed models.

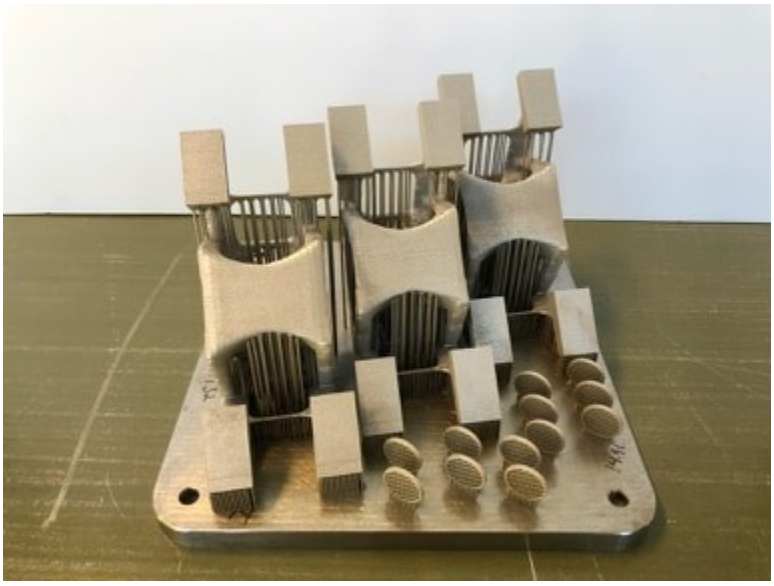

Figure 6.4 Upper view of the printed models.

CHAPTER VII

THREE-POINT BENDING TEST

This chapter presents the flexural bending tests of the printed structures. The smoothed designs were additively manufactured using the selective laser melting process; those structures are tested using the same boundary conditions of the three-point bending problem. The bending test employs a specific test fixture using a universal test machine. The three-point bending test is set based on the ASTM D790 standards for both material properties and dimensions.

In the three-point bending test, tensile stress is applied in the convex side of the specimen, whereas compressive stress is applied in the concave side inducing local shear stress through the midline of the structure. To make sure that the failure is due to the applied tensile stress or compressive stress, the induced local shear stress should be minimal. The flexural strength, which is the material's stiffness, is determined throughout the gathered data of the load-deflection curves. The flexural bending test provides essential data that describes the bending mechanism of the printed models based on load-deflection curves. Also, it allows determining the modulus of elasticity based on the bend test data. In beam theory, the three-point bend test is a classical problem used to study the bending mechanism of elastic structures. Flexural stiffness is related to Young's modulus via the maximum deflection formula at the midline of the beam. This test is conducted until reaching plastic deformation of the printed models.

$$\delta_{max} = \frac{PL^3}{48EI} \tag{7.1}$$

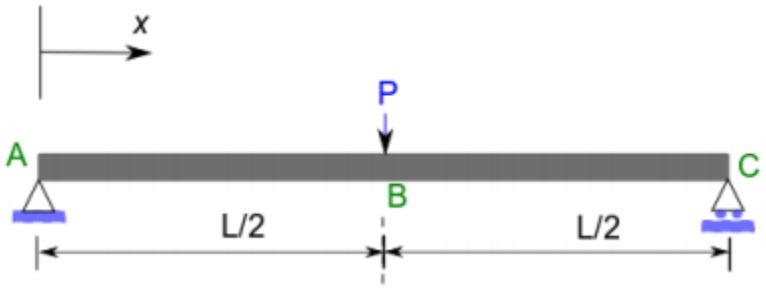

Figure 7.1 Three-point bending problem [58].

7.1 Experimental Set-up

The printed specimens were tested using INSTRON 5882 equipment with a capacity of 100 KN. The vertical displacement was measured using INSTRON'S extensometer. In order to have accurate bending results, the flexural behavior should be is induced either by tensile or compression stress, as mentioned before. This hypothesis is ensured based on the shear span to depth ratio of the tested structure [59].

Figure 7.2 INSTRON 5882 [60]

The bending test is conducted using a vertical displacement of 0.01 mm/sec. The supporting feet (figure 7.3) were designed to test the printed parts appropriately since the contact regions between the optimized beam models are too small to ensure a stable flexural bending test. The deflection of tested beams was measured using INSTRON's extensometer at the midline of the specimens. In the meantime, the load-deflection curves were recorded simultaneously throughout the test.

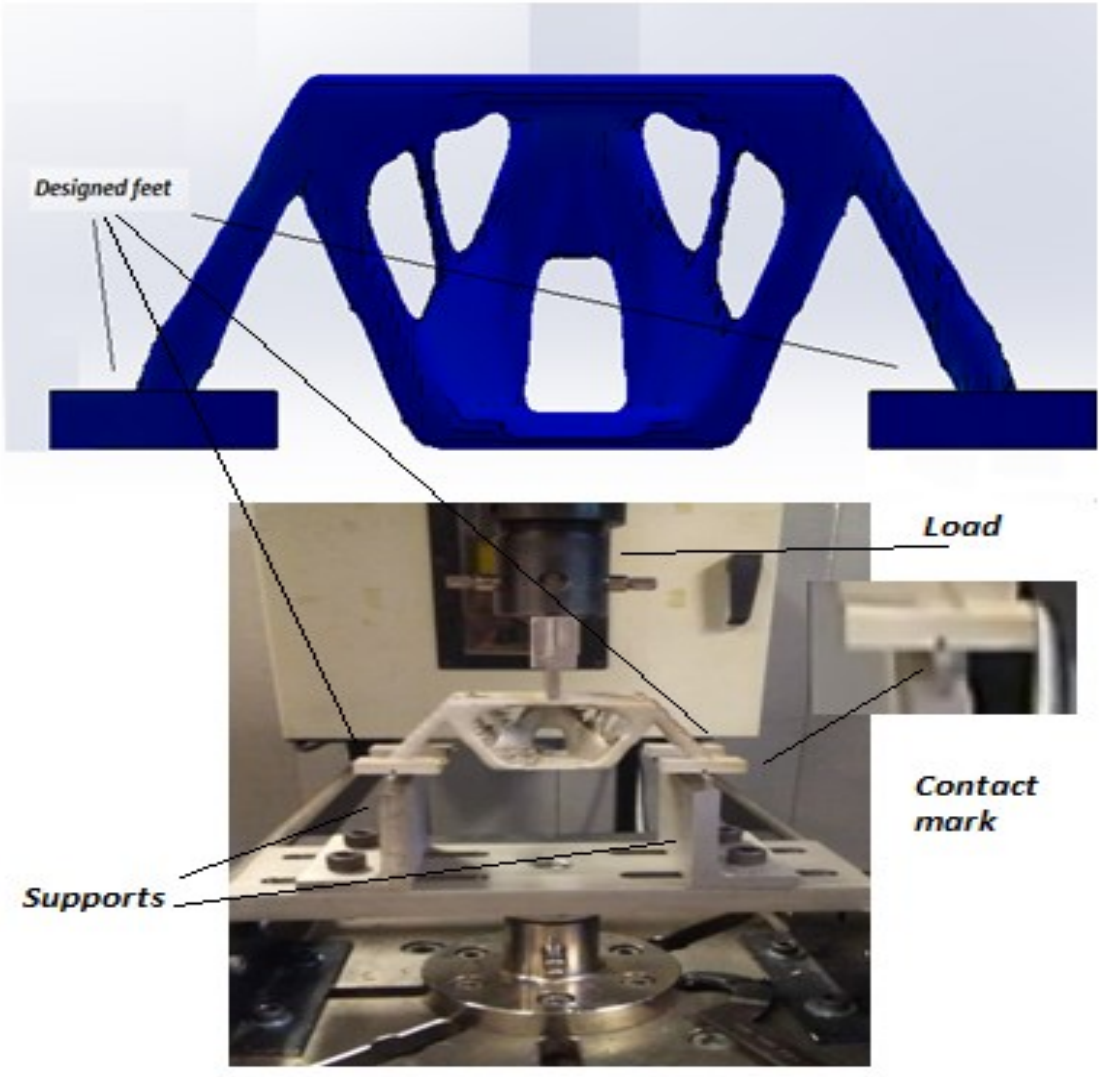

Figure 7.3 Illustration of the bending test.

The figure below illustrates the configuration used during the three-points bending test showing the contact regions of the specimen as well as the location of the applied load. The contact regions between the supports and the specimen were marked at the middle of the supporting feet to obtain an accurate flexural bending pattern as well as a precise measurement of deflection at the midline. The supports interact with the specimen at four locations; two in each side to stabilize the beam during the test.

7.2 Numerical Results

In this section, the results obtained from the finite element analysis related to the linear elastic regime are illustrated since we are interested in the linear elastic behavior of the printed models. The boundary conditions implemented in the numerical simulation are pinned-end contact at the left-hand side and a roller contact at the right-hand side; this approach illustrates well the behavior of the specimens like the ones observed during the experiment.

Since the numerical model is set to simulate the linear elastic behavior, the maximum stress does not exceed the elastic limit. The optimized model exhibits compressive stress at the upper part of the optimized beam, whereas the tensile stresses are situated at the lower part. Both observed stresses have significant effects on the flexural behavior of the optimized MBB-beam; which have to be taken into consideration while setting the optimization problem to obtain an optimized model capable of sustaining loads in a realistic environment.

Based on the linear behavior of the three-points bending equation, a straight line is plotted using the following formula:

$$\frac{dP}{d\delta} = \frac{48EI}{L^3} \tag{7.2}$$

E: Young's modulus

I: Moment of inertia

P: Load

L: Distance between supports

δ : Deflection

To plot the curve, we use the applied load of the numerical model as well as the obtained maximum deflection from the finite element analysis to determine the slope based on the numerical simulation. From the simulation, the deflection reached is 0.25 mm.

$$\frac{P}{\delta_{max}} = 26.452\ kN/mm \tag{7.3}$$

For further analysis, the linear elastic curve of the numerical model is added to the graphs containing the experimental curves and compare the obtained results in terms of flexural stiffness of each specimen.

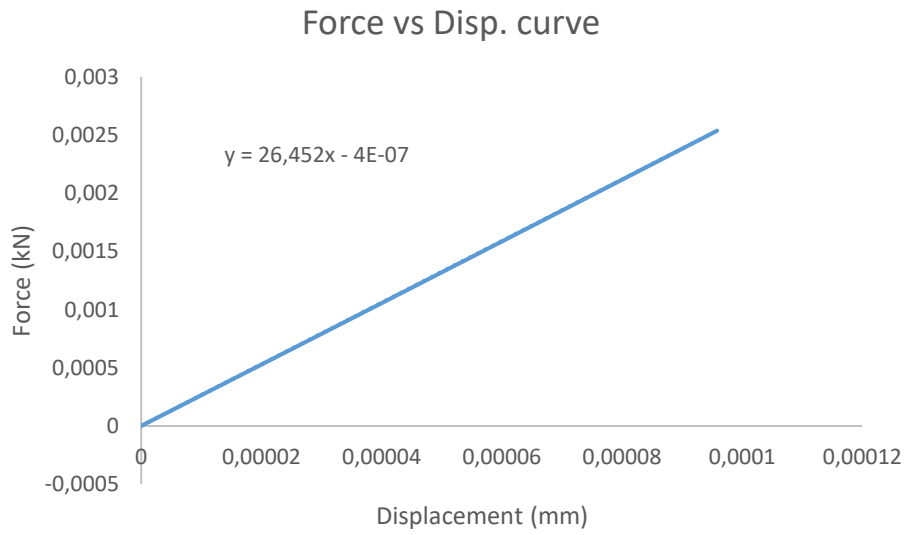

Figure 7.4 Load-deflection slope of the numerical model.

7.3 Experimental Results

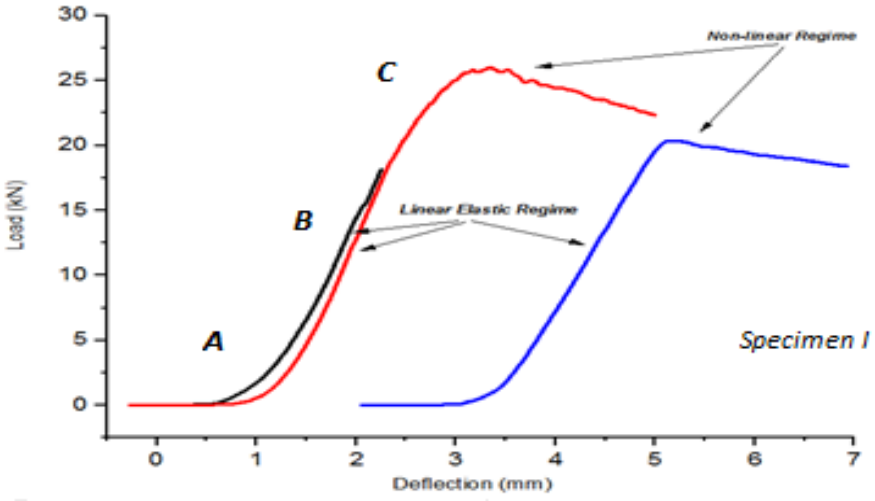

Figure 7.5 Load-deflection curves of the first experiment. Specimen I

Throughout the first experiment, three bending tests were conducted on the same specimen. Based on the graph of the first experiment, there are three regions:

- ***Region A:*** During this phase of the test, the specimen was seated on the testing platform and the vertical load application was initiated. The non-linear behavior in this region is explained by the effect of stability on the bending performance of the specimen.
- ***Region B:*** The linear elastic behavior of the specimen.
- ***Region C:*** The plastic deformation of the specimen.

The following experiment is divided into three sections by varying the applied load at different regimes to depict the behavior of the specimen. These tests intend to obtain the linear elastic zone and the plastic zone. The variation of the applied load rate established from a slower rate to a higher rate enabled the specimen to respond differently throughout the flexural bending tests.

During Test I, the specimen was incrementally subjected to a vertical load at the upper surface. The applied load reached a value of 18.03 KN equivalents to 2.15 mm in deflection; the specimen was unloaded when attaining its elastic limit prior deformation.

During Test II, the specimen was unloaded, allowing it to regain its initial shape since we have not exceeded the elastic limit of the specimen. At this level, the load is incremented at a different rate and exceeds the elastic limit of the specimen, allowing it to deform plastically. After reaching its maximum bending load of 25.99 KN, the load started decreasing almost in a linear form, whereas the deflection increased, reaching a value of 5 mm.

During Test III, the specimen was unloaded once more for a while before starting the test. The third test started nearly at 2.1 mm of deflection; the amount of deflection reached was induced by the plastic deformation observed within the second test. The applied load of the third test has not reached a higher value compared to test II. The deflection corresponding to the maximum applied load is 5.05 mm. After reaching its maximum value, the load started decreasing linearly, whereas the deflection increased, reaching a value of 6.9 mm.

Both experiments II and III were tested using the same following data inputs:

Table 7.2 Data inputs of experiment II and III.

Inputs	**Specimen label**	**Values**	
Dimension	Support span	137.19	mm
Dimension	Thickness	60.24	mm
Dimension	Width	72.66	mm
Test	Rate 1	0.01	mm/sec

For experiments II and III, the test was conducted under similar conditions of the first experiment. Although, the rate of the applied load was kept the same throughout the test until reaching its maximum bending load.

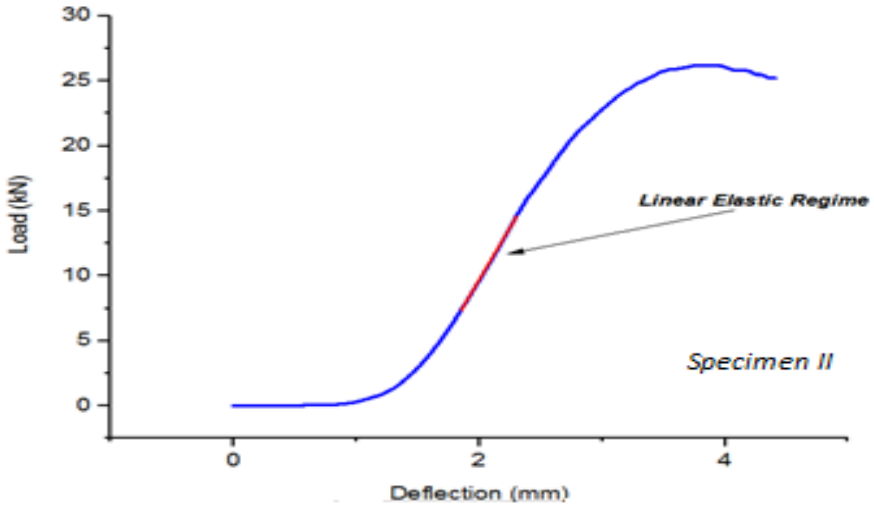

Figure 7.6 Load-deflection curve of the second experiment. Specimen II

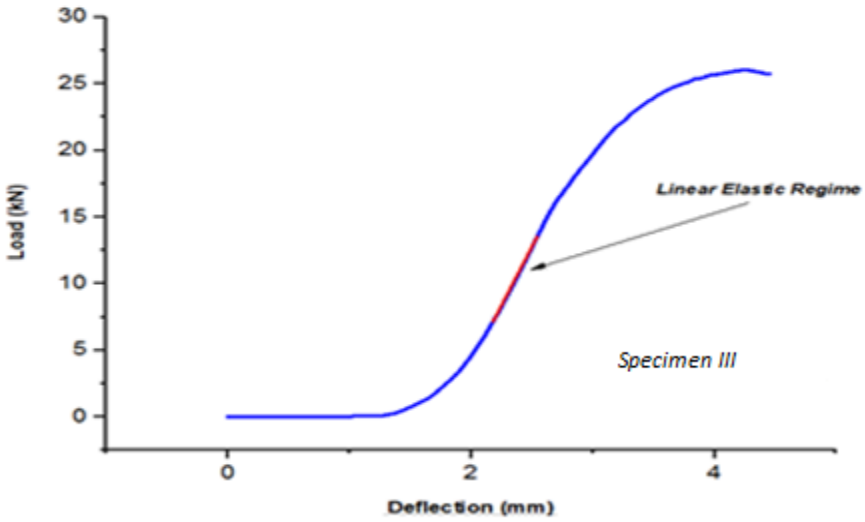

Figure 7.7 Load-deflection curve of the third experiment. Specimen III

Throughout the analysis, the curves of specimen I are the results obtained from test II of the first experiment.

The following experimental data were obtained from the INSTRON testing machine. Based on these results, the maximum bending load and the deflection at maximum bending load were extracted from the load-deflection curve.

Table 7.3 Results obtained from the three tests.

Specimen Type	***Maximum Bending Load (kN)***	***Deflection at maximum bending load (mm)***
Taubin smoothing – specimen I	25.99 kN	3.3515 mm
Taubin smoothing – specimen II – Test II	26.21 kN	3.8122 mm
Taubin smoothing – specimen III	26.002 kN	4.2819 mm

For the maximum bending load, it is noticeable based on the values of the table that the specimens have reached nearly the same range of the maximum load with slight differences especially specimen II which has the highest load of 26.21 kN exceeding specimen I with 220 N and specimen II with 208 N. For the deflection at maximum bending load, it is apparent from the table that specimen III has the most considerable amount of deflection followed by specimen II whereas specimen I has the lowest amount of deflection. Although the printed models are replicates of the same mesh smoothing method, their mechanical behavior throughout the flexural bending unveiled different structural properties. These differences are caused by the printing process; which influences the quality of the designed models since the relative density used during

the printing phase affects the flexural strength. Based on the flexural behavior of the parts, the load-deflection curve is composed of two mechanical regimes; a linear elastic regime which enables the specimen to regain its initial shape when unloaded as long as it has not exceeded the elastic limit and a plastic regime in which an irreversible deformation occurs.

Figure 7.8 Deformed part.

The apparent flexural deformations are due to the transition from the linear elastic regime to the plastic regime; these deflections occur mainly at the supporting feet and the midline section of the specimen. After exceeding the linear elastic regime, the applied load increases in the form of a parabola to reach its peak attaining the maximum deflection at the midline section. In fact, the occurred transition engendered a loss of stiffness, which can be interpreted by a significant compression at the upper surface as well as a high tension at the lower surface mostly at the

supporting feet. From the load-deflection curve, the plastic regime can be divided into two sections: a parabolic zone comprising fluctuations and an almost linear curve at the end.

The observed fluctuations are due to the vibrations resulting from the contact with the supports. The flexural behavior generated at the plastic regime increased significantly inducing high compression stress at the upper side and high tensile stress at the lower side, causing the supporting feet to slide on the supports. After the load drop, the specimen continued to sustain the applied load less than the peak. The non-linear behavior is due to the compressive yielding of the anisotropic microstructure of the layers.

Figure 7.9 Bending angle of the feet.

After attaining the maximum load of 25 KN, a critical compressive effect observed, causing the bending angle between the feet and the central part of the body to increase massively. Throughout the experimental test, the models have not reached the fracture point remaining close to the linear

elastic regime. Accordingly, a linear elastic analysis was conducted due to the incompleteness of the non-linear behavior of the specimen at the plastic regime based on the load-extension curve. Several mechanical properties of the tested samples were deduced such as energy absorbed till maximum load and energy absorbed till maximum deflection. The energy absorbed by each specimen was determined by integrating the area under the load-deflection curve.

Table 7.4 Experimental data of the three experiments.

Specimen Type	***Deflection at Maximum bending load (mm)***	***Energy absorbed till maximum load (J)***
Taubin smoothing – specimen I	3.3515 mm	0.006662848
Taubin smoothing – specimen II	3.8122 mm	0.013118
Taubin smoothing – specimen III	4.2819 mm	0.013085

Based on the obtained results, it is apparent that specimen II has absorbed more energy than both Specimen I and specimen II. Throughout the optimization process, the optimal material distribution is obtained by minimizing the overall compliance of the structure within a predefined design domain. Since compliance is the inverse of stiffness, the minimization of compliance within a structure increases stiffness. Moreover, the compliance of a structure is measured in strain energy within the linear elastic regime. In elasticity, it is called elastic strain energy. Strain energy is defined as the internal work done in deforming the body by the action of externally applied forces; it is the amount of potential energy stored due to deformation.

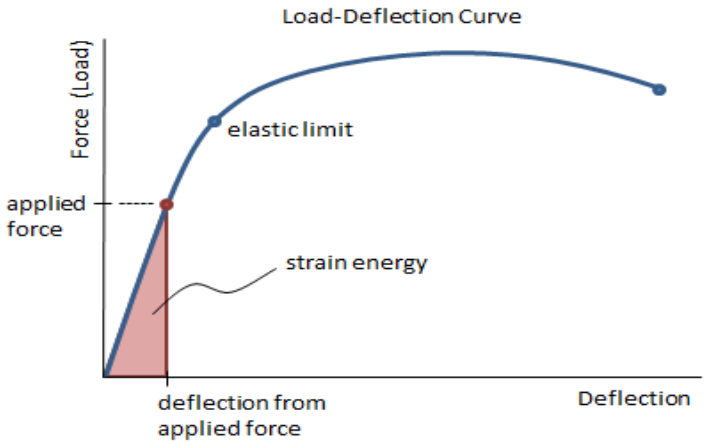

Figure 7.10 Illustration of strain energy [61].

Using the load-deflection curves, the linear elastic regime of each specimen. From the linear elastic regime, the elastic strain energy is determined by integrating over the load-deflection area within the elastic limit.

Table 7.5 Elastic strain energy of each specimen.

Specimen Type	***Elastic strain energy (kN.mm)***
Specimen I	8.99893
Specimen II	8.21572
Specimen III	7.62255

The purpose of this plot is to compare the value of flexural stiffness at the linear elastic regime of each specimen. The flexural stiffness measures the resistance of a specimen when subjected to bending deformation. A high value of the flexural stiffness factor means that the structure has fewer tendencies to deflect or bend.

Table 7.6 Flexural modulus of the three tested specimens.

Specimen	Specimen I	Specimen II	Specimen III
Flexural Stiffness (kN/mm)	20.51	15.21	16.3

7.4 Discussion

A comparative analysis is set between the linear-elastic curve of the numerical model and the experimental data. For further examination, the linear-elastic portion of the numerical model was added to the previous load-deflection plots. The purpose of this analysis is to examine the flexural behavior of the printed beams throughout the bending tests and assess the main causes behind the difference in flexural stiffness.

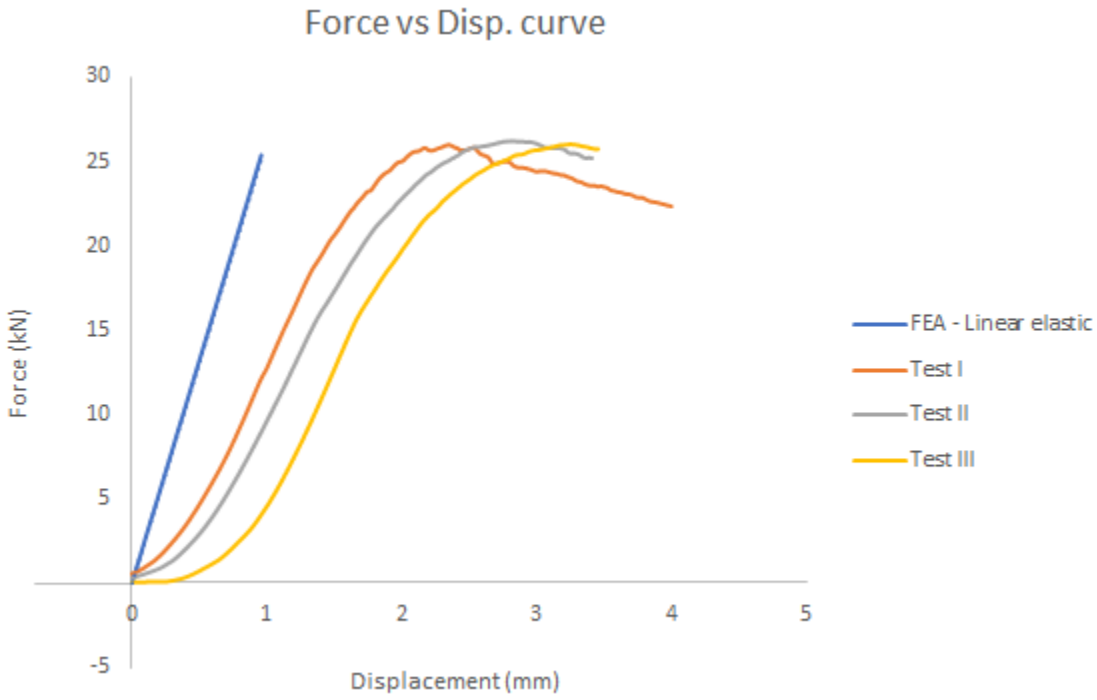

Figure 7.11 Numerical and experimental curves of the comparative analysis.

Table 7.7 Values of flexural stiffness of the numerical and the experimental model.

	Numerical model	**Experimental model**
Flexural stiffness (kN/mm)	26.452	20.51

For the experimental models, we have considered the highest flexural stiffness value, which is 20.51 kN/mm; since the slope (flexural stiffness) is not the same within the elastic region due to the obtained non-linearity. Based on the curves, specimen I have the highest flexural stiffness compared to specimen II and specimen III. The high flexural stiffness of the experimental model can be explained by the anisotropic microstructure, which is not the case for the CAD model. The CAD model is assumed to have an isotropic behavior. Also, the modeled supports did not have the exact same effect as the one observed during the experiment. Since the numerical model is considered isotropic several geometric imperfections are not considered throughout the finite element analysis. In addition, the printed models suffered from residual stresses and porosity. The numerical model considered the variation of Young's modulus throughout the selective laser melting process; based on previous researches done on the behavior of the mechanical properties of stainless steel 316l. Since the printed parts used a specific build orientation, the Young's modulus used was in accordance to the build angle. The obtained results showed that the finite element analysis predicted the range of the flexural stiffness.

The apparent difference between specimen I, II, and III is the energy dissipated due to material internal friction. It is noticeable that the flexural stiffness of the three tests is slightly different even though the tested specimens are replicates; this hypothesis is clear when we compare both specimens I and III. One of the reasons behind the difference in flexural stiffness is the change

in the line of the applied load during the yielding of the parts. In fact, as the tested part started deflecting downwards; the perpendicular application of the load shifted slightly at the upper surface.

The main reason behind the difference in flexural stiffness between the experimental and numerical model is related to the dissimilarity of the mechanical properties within the microstructure. In fact, the additive manufacturing process is affected by several parameters that affect the mechanical properties of the printed parts. The manufactured parts were sliced using specific parameters; each slice has a predefined height that influences the infill percentage of the superposed layers. In addition, the layer-by-layer build induces road gaps and air-voids within the microstructure. The layered raster imposed a specific direction during the building process that orients the stainless-steel 316l molecules within the microstructure, which impacts the flexural resistance of the parts in certain directions [62].

Figure 7.12 Apparent layers.

Several parameters did affect the flexural stiffness during the building process of the optimized models such as the laser power, laser scan speed as well as the relative density. These factors influence the mechanical properties of the printed specimen throughout their microstructure, surface quality and toughness. The breaking stress, hardness, lengthening and the elastic yield point are majorly affected by the printing process [63].

Figure 7.13 Remaining supports.

The following figure shows the remaining supports of the part. These supports are used to print complex regions within the structure. The built supports did affect the flexural behavior of the specimens by inducing an asymmetry because most of them were located the right-hand side of the parts. This asymmetry appeared clearly throughout specimen I, which exhibited a flexural bending towards the left-hand side. These supports require additional machining to be subtracted from the surface. Moreover, the supports had different impacts on the geometry of the manufactured parts. For instance, the specimen I had an apparent formation of residual stresses at the supporting feet.

Also, the thickness of the supports induced shape deformations at the sharp corners of the parts. Observing the manufactured parts, some minor supports were built in the middle of the structures; linking multiple regions. The links engendered additional flexural resistance to the parts.

Figure 7.14 Minor bridge.

The observed bridges influenced the bending mechanism by restraining the linked regions, which required a consistent load application to force the tensile behavior. These geometric inconsistencies induced additional local shear stresses within the structures. The Local shear stresses accentuated the effect of the geometric non-linearity by inducing small oscillations due to the vibrational effect of the bending load.

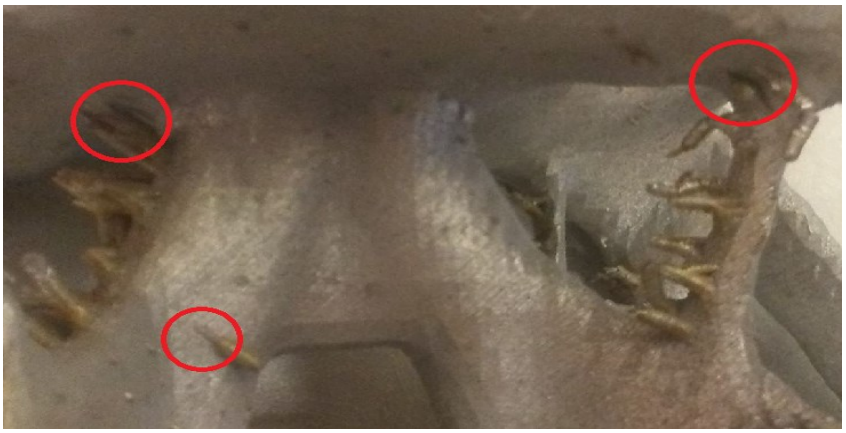

Figure 7.15 Multiple bridges.

The infill percentage affects the stiffness of the built layers since it controls the amount of material melted following the laser's path. The infill engenders local porosity within neighboring layers. The induced porosity causes the microstructure to lose its strength and behave in a non-linear manner [64]. The transformation of energy and mass during the melting process is manifested through absorption and scattering of laser radiation. The selective laser melting process exhibit high thermal behavior that engenders shape distortions and residual stresses. The accumulation of the high-temperature process generates fatigue failure due to the reduction in the geometrical accuracy of the printed parts [65].

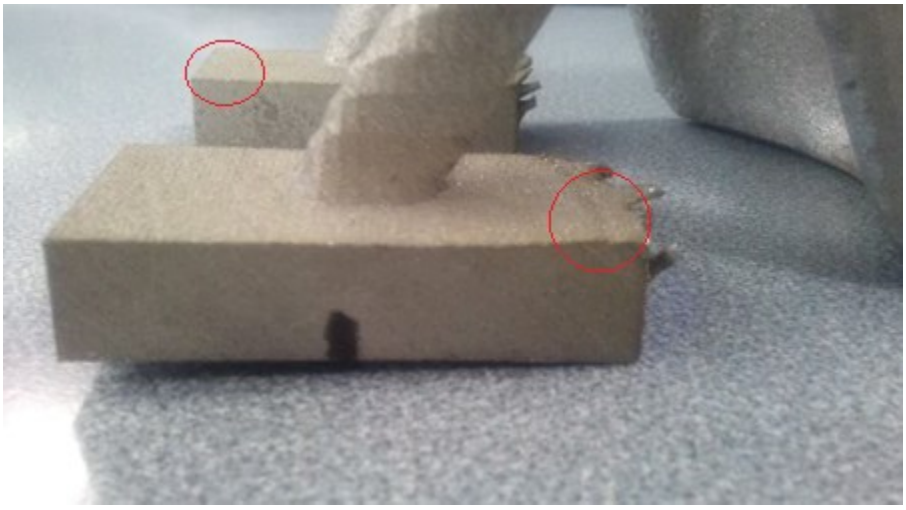

Figure 7.16 Shape distortions.

The shape distortions induced geometric non-linearity throughout the bending test.

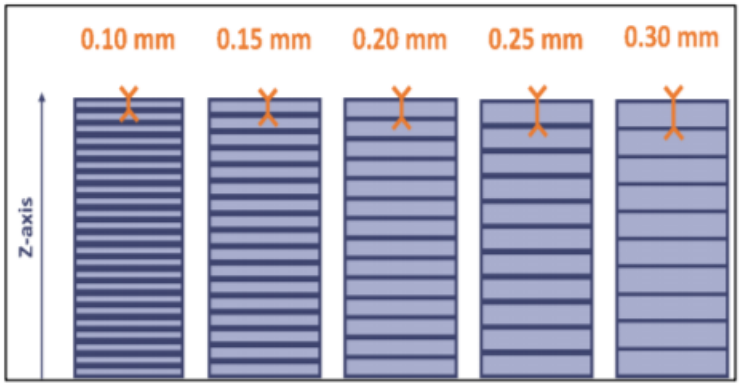

Figure 7.17 Variation of the layer's height [66].

During the layer-by-layer building process, it is essential to define the height of each melted layer. Based on the chosen height, the slicing feature characterizes each region by its estimated number of layers. Since the infill percentage plays a major role on the formation of highly porous layers, it is critical to find an optimal number of layers to reduce the void gaps that encounter the layering process [67]. Increasing the number of layers induces more microstructural discontinuities that weakens the layer adherence within the structure, which affects the tensile strength. In fact, the gap between the layers should be minimized to obtain a highly bonded microstructure providing optimal mechanical properties of the melted material. The contact between the layers during the melting process engenders inter-molecular diffusivity due to the heat transfer within the build chamber [68]. Furthermore, the selective laser melting process uses a laser scanning strategy that controls the grain orientation within the microstructure. Throughout the melting process, both rapid heating and cooling affects the flowability of the melted material preventing the formation of a uniform density distribution. The powder flowability is vital during the melting process it affects the quality of the built layers [69]. Also, the inter-molecular forces between the molecules influence the distribution of particles within the microstructure.

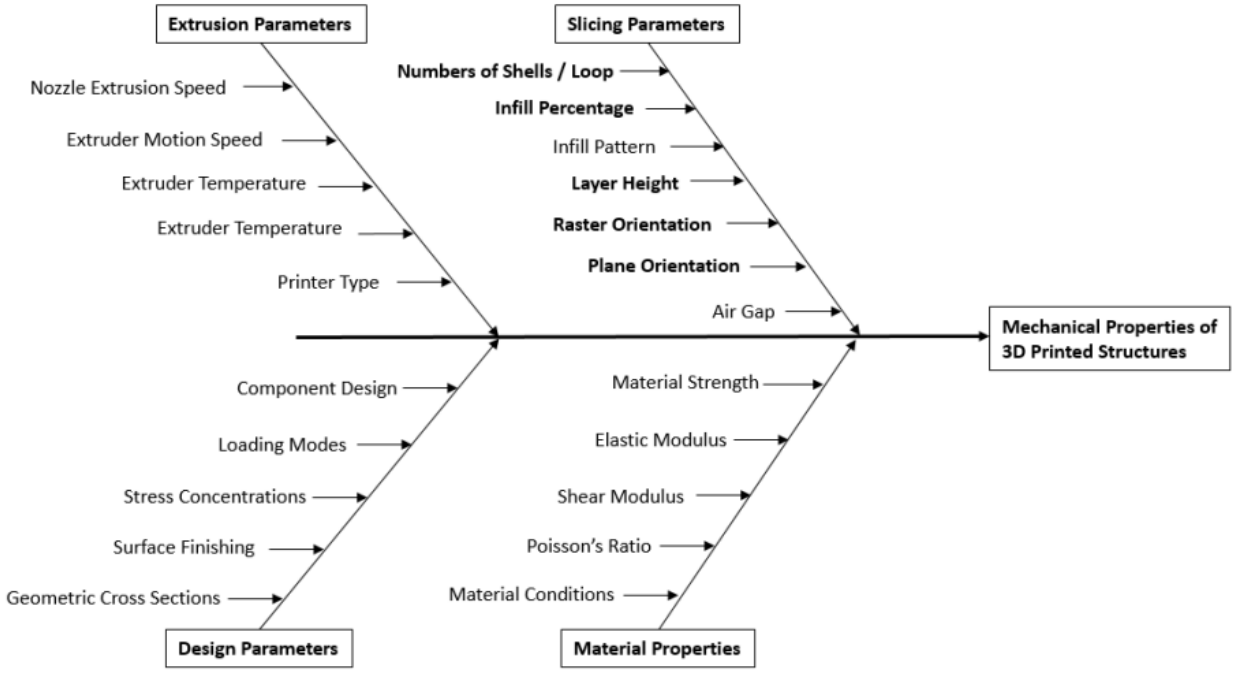

Figure 7.18 Influential parameters of additive manufacturing [70].

Several parameters did affect the flexural stiffness during the building process of the optimized models such as the laser power, laser scan speed as well as the relative density. These factors influence the mechanical properties of the printed specimen throughout their microstructure, surface quality and toughness. The breaking stress, hardness, lengthening and the elastic yield point are majorly affected by the printing process.

7.5 Potential causes

In this part, multiple factors are discussed to elucidate the difference obtained in flexural bending stiffness between numerical and experimental results. It is essential to examine the main aspects that affected the flexural behavior of the numerical model as well as the built part. A modelling strategy is required to predict accurately the structural performance of additively manufactured parts. Thus, it is necessary to elaborate a concise methodology to model additively manufactured structures to achieve results capable of predicting the overall performance in real applications. The major causes are:

- The experiment model was manufactured using layer-by-layer approach compared to the CAD model.
- In the numerical model, the applied material does not take into consideration the microstructure's anisotropy, which is induced throughout the selective laser melting process.
- The build orientation affects the mechanical properties such as Young's modulus, hardness and yield strength. The Young's modulus depends on the build angle.
- Due to the thermal activity of the selective laser melting process, residual stresses induce geometric inconsistencies and discontinuities within the manufactured parts. These anomalies engender a significant deviation in flexural stiffness between the built model and the CAD model.

7.6 Conclusions

Throughout this work, an optimized MBB-beam was modeled, manufactured and tested to evaluate the bending mechanism and the effect of the selective laser melting process on the mechanical properties of additively manufactured parts. This framework integrates topology optimization into the additive manufacturing process, and it implements Taubin mesh smoothing technique within the design to attenuate geometric noises within meshes in order to reduce the formation of overhanging angles and residual stresses due to the thermal activity of the additive manufacturing process.

- One of the most common optimization techniques is Solid Isotropic Material with Penalization (SIMP), this method uses a method of density penalization that guides the final solution to a significant formation (0 and 1) by eliminating irrelevant densities within the structure. Based on the SIMP MATLAB code, the optimization problem obeys a density-based approach using a modified SIMP interpolation method, which involves independency of the penalization power, and the minimum Young's modulus. Since the density-based approach relies on relaxing the binary problem by implementing a continuous density value, the overall material distribution depends on the material density distribution. A minimum compliance analysis was applied to enhance the overall integrity of the structure by minimizing its total strain energy in order to obtain a stiff optimized model.
- After solving the optimization problem, the optimized model was smoothed using Taubin method. The smoothed versions using the Taubin smoothing method were additively manufactured using selective laser melting technique.

- A flexural bending experiment was conducted using the three points bending test to validate the design requirements of the numerical model and depict the behavior of the optimized model in terms of strain energy and displacement. In fact, the bending test of the manufactured model unveiled satisfactory results that confirmed the design requirements of the obtained numerical optimization model. The performed design methodology allowed complex optimized models to be additively manufactured by integrating a powerful tool such as mesh smoothing technique, which reduced the formation of overhanging angles and residual stresses that could occur during the laser melting process.
- After obtaining the numerical results via optimization codes in. STL format, comes the part where the resulted meshes has to be investigated in order to correct the problems that could occur when generating the final results through MATLAB. The most common problems that could be encountered in this case are surface gaps or misplaced facets, non-manifold vertices, degenerate facets and intersecting facets. These errors commonly exist in solid models due to imprecise arithmetic resolutions of geometries and programming inconsistencies. These types of errors obstruct critical analyses of solid models such as finite element analysis and rapid prototyping. The repair process used throughout the project is the import diagnostics feature on ABAQUS.
- After resolving the geometric errors of the meshes, a finite element analysis was undertaken using the same boundary conditions and the load application implemented during the three points bending test. A comparison between the mesh smoothing techniques in terms of stress distribution though the overall smoothed

structures and the in meantime validate the designed supporting feet and evaluate their integrity before experimentally testing the models.

- The Taubin smoothing operates using λ operator to adjust the inward diffusion and the μ operator to adjust the outward diffusion step also it uses a second order filter with a pass band gain to avoid the shrinkage of low frequency elements. In other means, the Taubin smoothing attenuates the mesh noises by preserving the same position of the smoothed surface.
- During the additive manufacturing process, the directional constraints were taken into consideration such as the printing direction which affects majorly the design quality, it was important during the printing phase to define an optimal print direction. As a result of the thermal activity within the additive manufacturing process; residual stresses are induced due to local melting and nonuniform cooling of the manufactured design. Indeed, support structures are implemented because of residual stresses and heat dissipation; in order to reduce these effects through the manufacturing process.

REFERENCES

[1] Gibson, I., Rosen, D., and Stucker, B. (2015). Additive Manufacturing Technologies. [Elektronisk resurs]: 3D Printing, Rapid Prototyping, and Direct Digital Manufacturing. New York, NY: Springer New York: Imprint: Springer, 2015.

[2] Christensen, P. W., Gladwell, G. M. L., and Klarbring, A. (2008). An introduction to structural optimization. Solid Mechanics and Its Applications: 153. Dordrecht: Springer Netherlands, 2008.

[3] Clausen, A. (2016). Topology Optimization for Additive Manufacturing. PhD thesis, Technical University of Denmark.

[4] I. N. Rozvany, George & Lewiński, T. (2014). Topology Optimization in Structural and Continuum Mechanics. 10.1007/978-3-7091-1643-2.

[5] I. N. Rozvany, George & Lewiński, T. (2014). Topology Optimization in Structural and Continuum Mechanics. 10.1007/978-3-7091-1643-2.

[6] I. N. Rozvany, George & Lewiński, T. (2014). Topology Optimization in Structural and Continuum Mechanics. 10.1007/978-3-7091-1643-2.

[7] D. Systems, “Topology and shape Optimization with Abaqus”, DS Simulia, Michigan,2011.

[8] Bendsøe, M.P. and Sigmund, O. (2003). Topology Optimization: Theory, Method and Application. Berlin: Springer.

[9] Bendsoe, M. P., & Kikuchi, N. (1988). Generating Optimal Topologies in Structural Design Using a Homogenization Method. Computer Methods in Applied Mechanics and Engineering, 71(2), 197-224. doi:Doi 10.1016/0045-7825(88)90086-2

[10] Bendsøe, Martin & Sigmund, Ole. (2003). Topology Optimization: Theory, Method and Applications.

[11] Bendsøe, M.P., “Optimal shape design as a material distribution problem,” Structural Optimization 1. 193-202. 1989.

[12] Steffen Johnsen. Structural Topology Optimization. (June),2013.

[13] Liu, K. & Tovar, A. Struct Multidisc Optim (2014) 50: 1175. https://doi.org/10.1007/s00158-014-1107-x

[14] Diaz, A. and Sigmund, O., "Checkerboard layouts in pattern optimization," Structural Optimization. 10:40-45, 1995.

[15] Bendsøe, M.P. and Sigmund, O., "Topology Optimization," Springer-Verlag, 2004.

[16] Liu, K. & Tovar, A. Struct Multidisc Optim (2014) 50: 1175. https://doi.org/10.1007/s00158-014-1107-x page:1187.

[17] M. P. Bendsøe, Optimal shape design as a material distribution problem, Structural Optimization 1, 193 (1989).

[18] Liu, K. & Tovar, A. Struct Multidisc Optim (2014) 50: 1175. https://doi.org/10.1007/s00158-014-1107-x page:1176.

[19] Liu, K. & Tovar, A. Struct Multidisc Optim (2014) 50: 1175. https://doi.org/10.1007/s00158-014-1107-x page:1177.

[20] Razvan Cazacu and Lucian Grama. Overview of structural topology optimization methods for plane and solid structures. Annals of the University of Oradea, (December), 2014.

[21] Liu, K. & Tovar, A. Struct Multidisc Optim (2014) 50: 1175. https://doi.org/10.1007/s00158-014-1107-x page:1186.

[22] Liu, K. & Tovar, A. Struct Multidisc Optim (2014) 50: 1175. https://doi.org/10.1007/s00158-014-1107-x page:1177.

[23] Liu, K. & Tovar, A. Struct Multidisc Optim (2014) 50: 1175. https://doi.org/10.1007/s00158-014-1107-x page:1177.

[24] Liu, K. & Tovar, A. Struct Multidisc Optim (2014) 50: 1175. https://doi.org/10.1007/s00158-014-1107-x page:1178.

[25] Liu, K. & Tovar, A. Struct Multidisc Optim (2014) 50: 1175. https://doi.org/10.1007/s00158-014-1107-x page:1179.

[26] Liu, K. & Tovar, A. Struct Multidisc Optim (2014) 50: 1175. https://doi.org/10.1007/s00158-014-1107-x page:1179.

[27] Liu, K. & Tovar, A. Struct Multidisc Optim (2014) 50: 1175. https://doi.org/10.1007/s00158-014-1107-x page:1179.

[28] Liu, K. & Tovar, A. Struct Multidisc Optim (2014) 50: 1175. https://doi.org/10.1007/s00158-014-1107-x page:1185.

[29] Liu, K. & Tovar, A. Struct Multidisc Optim (2014) 50: 1175. https://doi.org/10.1007/s00158-014-1107-x page:1185.

[30] Liu, K. & Tovar, A. Struct Multidisc Optim (2014) 50: 1175. https://doi.org/10.1007/s00158-014-1107-x page:1177.

[31] Liu, K. & Tovar, A. Struct Multidisc Optim (2014) 50: 1175. https://doi.org/10.1007/s00158-014-1107-x page:1188.

[32] Ohtake, Yutaka & Belyaev, Alexander & Bogaevski, I.A. (2000). Polyhedral surface smoothing with simultaneous mesh regularization. Geometric Modeling and Processing. 229 - 237. 10.1109/GMAP.2000.838255.

[33] D. Brackett, I. Ashcroft, R. Hague,Topology optimization for additive manufacturing. In Proceedings of the solid freeform fabrication symposium, 1 (2011) 348-362.

[34] https://help.solidworks.com/2018/English/SolidWorks/sldworks/c_ Import_Diagnostics_Overview.htm

[35] K. F. leong, C. K. Chua and Y. M. Ng, "A study of stereolithography files and Repair. part 1.," The international journal of Additive manufacturing Technology, vol. 12, pp. 407-414, 1996.

[36] K. F. leong, C. K. Chua and Y. M. Ng, "A study of stereolithography files and Repair. part 1.," The international journal of Additive manufacturing Technology, vol. 12, pp. 407-414, 1996.

[37] K. F. leong, C. K. Chua and Y. M. Ng, "A study of stereolithography files and Repair. part 1.," The international journal of Additive manufacturing Technology, vol. 12, pp. 407-414, 1996.

[38] K. F. leong, C. K. Chua and Y. M. Ng, "A study of stereolithography files and Repair. part 1.," The international journal of Additive manufacturing Technology, vol. 12, pp. 407-414, 1996.

[39] K. F. leong, C. K. Chua and Y. M. Ng, "A study of stereolithography files and Repair. part 1.," The international journal of Additive manufacturing Technology, vol. 12, pp. 407-414, 1996.

[40] Merkt, S.J. Qualifizierung von Generativ Gefertigten Gitterstrukturen für maßgeschneiderte Bauteilfunktionen. Ph.D. Thesis, RWTH Aachen, Aachen, Germany, 2015.

[41] Merkt, S.J. Qualifizierung von Generativ Gefertigten Gitterstrukturen fürmaßgeschneiderte Bauteilfunktionen. Ph.D. Thesis, RWTH Aachen, Aachen, Germany,2015.

[42] https://hawkridgesys.com/blog/solidworks-simulation-curvature-based-vs-standard-mesher

[43] Gibson, I., Rosen, D., and Stucker, B. (2015). Additive Manufacturing Technologies. [Elektronisk resurs]: 3D Printing, Rapid Prototyping, and Direct Digital Manufacturing. New York, NY: Springer New York: Imprint: Springer, 2015.

[44] https://en.wikipedia.org/wiki/3D_printing#Terminology

[45] Clausen, A. (2016). Topology Optimization for Additive Manufacturing. PhD thesis, Technical University of Denmark.

[46] Gardan, J. (2016). Additive manufacturing technologies: state of the art and trends. International Journal of Production Research, 54(10):3118-3132.

[47] Gardan, J. (2016). Additive manufacturing technologies: state of the art and trends. International Journal of Production Research, 54(10):3118-3132.

[48] Li, C., Liu, J., and Guo, Y. (2016). Prediction of residual stress and part distortion in selective laser melting. Procedia CIRP, 45:171-174. 3rd CIRP Conference on Surface Integrity.

[49] Leary, M., Merli, L., Torti, F., Mazur, M., and Brandt, M. (2014). Optimal topology for additive manufacture: A method for enabling additive manufacture of support-free optimal structures. Materials and Design, 63(1):678.

[50] Langelaar, M. (2017). An additive manufacturing filter for topology optimization of print ready designs. Structural and Multidisciplinary Optimization, 55(3):871-883.

[51] Shutian, L., Quhao, L., Wenjiong, C., Liyong, T., and Gengdong, C. (2015). An identi-cation method for enclosed voids restriction in manufacturability design for additive manufacturing structures. Frontiers of Mechanical Engineering, 10(2):126-137.

[52] Quhao, L., Wenjiong, C., Shutian, L., and Liyong, T. (2016). Structural topology optimization considering connectivity constraint. Structural and Multidisciplinary Optimization, 54(4):971-984.

[53] Poulsen, T. A. (2003). A new scheme for imposing a minimum length scale in topology optimization. International Journal for Numerical Methods in Engineering, 57(6):741-760.

[54] Zhou, M., Lazarov, B., Wang, F., and Sigmund, O. (2015). Minimum length scale in topology optimization by geometric constraints. Computer Methods in Applied Mechanics and Engineering, 293:266-282.

[55] Gibson, I., Rosen, D., and Stucker, B. (2015). Additive Manufacturing Technologies. [Elektronisk resurs]: 3D Printing, Rapid Prototyping, and Direct Digital Manufacturing. New York, NY : Springer New York : Imprint : Springer, 2015.

[56] https://resources.renishaw.com/en/details/data-sheet-ss-316l-0407-powder-for-additive-manufacturing--90802

[57] Gibson, I., Rosen, D., and Stucker, B. (2015). Additive Manufacturing Technologies. [Elektronisk resurs]: 3D Printing, Rapid Prototyping, and Direct Digital Manufacturing. New York, NY : Springer New York : Imprint : Springer, 2015.

[58] http://mi.eng.cam.ac.uk/IALego/bender_files/bend_theory.pdf - figure1

[59] Hu, Biao & Wu, Yufei. (2018). Effect of shear span-to-depth ratio on shear strength components of RC beams. Engineering Structures. 168. 770-783. 10.1016/j.engstruct.2018.05.017.

[60] https://icme.hpc.msstate.edu/mediawiki/index.php/File:Instron_5882.JPG

[61] https://mechanicalc.com/reference/mechanical-properties-of-materials - strain energy

[62] Rodríguez-Panes, A., Claver, J., & Camacho, A. M. (2018). The Influence of Manufacturing Parameters on the Mechanical Behaviour of PLA and ABS Pieces Manufactured by FDM: A Comparative Analysis. Materials (Basel, Switzerland), 11(8), 1333. doi:10.3390/ma11081333

[63] Stoia, Dan & Linul, Emanoil & Marsavina, Liviu. (2019). Influence of Manufacturing Parameters on Mechanical Properties of Porous Materials by Selective Laser Sintering. Materials. 12. 871. 10.3390/ma12060871.

[64] L. Mugwagwa, D. Dimitrov, S. Matope, I. Yadroitsev, Influence of process parameters on residual stress related distortions in selective laser melting, Procedia Manufacturing, Volume 21, 2018, Pages 92-99, ISSN 2351-9789,

[65] L. Mugwagwa, D. Dimitrov, S. Matope, I. Yadroitsev, Influence of process parameters on residual stress related distortions in selective laser melting, Procedia Manufacturing, Volume 21, 2018, Pages 92-99, ISSN 2351-9789,

[66] http://my3dmatter.com/wp-content/uploads/2015/03/layerheightimage.png

[67] Fernandez-vicente, Miguel & Calle, Wilson & Ferrándiz, S. & Conejero, Andres. (2016). Effect of Infill Parameters on Tensile Mechanical Behavior in Desktop 3D Printing. 3D Printing and Additive Manufacturing. 3. 183-192. 10.1089/3dp.2015.0036.

[68] Mirkoohi, E., Seivers, D. E., Garmestani, H., & Liang, S. Y. (2019). Heat Source Modeling in Selective Laser Melting. Materials (Basel, Switzerland), 12(13), 2052. doi:10.3390/ma12132052

[69] Spierings, A.B., Voegtlin, M., Bauer, T. et al. Prog Addit Manuf (2016) 1: 9. https://doi.org/10.1007/s40964-015-0001-4

[70] https://hackaday.io/project/12439-fdmproperties

[71] https://top3dapp.com

APPENDIX A

MATLAB SCRIPTS

A.1 3D SIMP Matlab code courtesy of Liu and Tovar 2014.

```
% AN 169 LINE 3D TOPOLOGY OPITMIZATION CODE BY LIU AND TOVAR (JUL 2013)
function MOP = top3d14(nelx,nely,nelz,volfrac,penal,q,rmin)
% USER-DEFINED LOOP PARAMETERS
maxloop = 15;    % Maximum number of iterations
tolx = 0.01;      % Terminarion criterion
displayflag = 0;  % Display structure flag
% USER-DEFINED MATERIAL PROPERTIES
E0 = 190e9;           % Young's modulus of solid material
Emin = 1e-9;      % Young's modulus of void-like material
nu = 0.265;         % Poisson's ratio
% USER-DEFINED LOAD DOFs
il = nelx/2; jl = nely; kl = nelz/2;                 % Coordinates
loadnid = kl*(nelx+1)*(nely+1)+il*(nely+1)+(nely+1-jl); % Node IDs
loaddof = 3*loadnid(:) - 1;                              % DOFs
% USER-DEFINED SUPPORT FIXED DOFs
iif = [0 0 nelx nelx]; jf = [0 0 0 0]; kf = [0 nelz 0 nelz]; % Coordinates
fixednid = kf*(nelx+1)*(nely+1)+iif*(nely+1)+(nely+1-jf); % Node IDs
fixeddof = [3*fixednid(:); 3*fixednid(:)-1; 3*fixednid(:)-2]; % DOFs
% PREPARE FINITE ELEMENT ANALYSIS
nele = nelx*nely*nelz;
ndof = 3*(nelx+1)*(nely+1)*(nelz+1);
F = sparse(loaddof,1,-1,ndof,1);
U = zeros(ndof,1);
freedofs = setdiff(1:ndof,fixeddof);
KE = lk_H8(nu);
nodegrd = reshape(1:(nely+1)*(nelx+1),nely+1,nelx+1);
nodeids = reshape(nodegrd(1:end-1,1:end-1),nely*nelx,1);
nodeidz = 0:(nely+1)*(nelx+1):(nelz-1)*(nely+1)*(nelx+1);
nodeids = repmat(nodeids,size(nodeidz))+repmat(nodeidz,size(nodeids));
edofVec = 3*nodeids(:)+1;
edofMat = repmat(edofVec,1,24)+ ...
    repmat([0 1 2 3*nely + [3 4 5 0 1 2] -3 -2 -1 ...
    3*(nely+1)*(nelx+1)+[0 1 2 3*nely + [3 4 5 0 1 2] -3 -2 -1]],nele,1);
iK = reshape(kron(edofMat,ones(24,1))',24*24*nele,1);
jK = reshape(kron(edofMat,ones(1,24))',24*24*nele,1);
% PREPARE FILTER
iH = ones(nele*(2*(ceil(rmin)-1)+1)^2,1);
jH = ones(size(iH));
sH = zeros(size(iH));
k = 0;
for k1 = 1:nelz
    for i1 = 1:nelx
        for j1 = 1:nely
            e1 = (k1-1)*nelx*nely + (i1-1)*nely+j1;
            for k2 = max(k1-(ceil(rmin)-1),1):min(k1+(ceil(rmin)-1),nelz)
                for i2 = max(i1-(ceil(rmin)-1),1):min(i1+(ceil(rmin)-1),nelx)
                    for j2 = max(j1-(ceil(rmin)-1),1):min(j1+(ceil(rmin)-
1),nely)
                        e2 = (k2-1)*nelx*nely + (i2-1)*nely+j2;
                        k = k+1;
```

```
                        iH(k) = e1;
                        jH(k) = e2;
                        sH(k) = max(0,rmin-sqrt((i1-i2)^2+(j1-j2)^2+(k1-
k2)^2));
                    end
                end
            end
        end
    end
end
H = sparse(iH,jH,sH);
Hs = sum(H,2);
% INITIALIZE ITERATION
x = repmat(volfrac,[nely,nelx,nelz]);
xPhys = x;
loop = 0;
change = 1;
% START ITERATION
while change > tolx && loop < maxloop
    loop = loop+1;
    if loop <= 15, q=1;
    else
    q = min(2,1.01*q);
    end
    % FE-ANALYSIS
    sK = reshape(KE(:)*(Emin+xPhys(:)'.^penal*(E0-Emin)),24*24*nele,1);
    K = sparse(iK,jK,sK); K = (K+K')/2;
    tolit = 1e-8;
    maxit = 8000;
    M = diag(diag(K(freedofs ,freedofs)));
    U(freedofs,:)= pcg(K(freedofs ,freedofs) ,F(freedofs ,:),tolit,maxit,M);
    % OBJECTIVE FUNCTION AND SENSITIVITY ANALYSIS
    ce = reshape(sum((U(edofMat)*KE).*U(edofMat),2),[nely,nelx,nelz]);
    c = sum(sum(sum((Emin+xPhys.^penal*(E0-Emin)).*ce)));
    dc = -penal*(E0-Emin)*xPhys.^(penal-1).*ce;
    dv = ones(nely,nelx,nelz);
    % FILTERING AND MODIFICATION OF SENSITIVITIES
    dc(:) = H*(dc(:)./Hs);
    dv(:) = H*(dv(:)./Hs);
    % OPTIMALITY CRITERIA UPDATE
    l1 = 0; l2 = 1e9; move = 0.2;
    while (l2-l1)/(l1+l2) > 1e-3
        lmid = 0.5*(l2+l1);
        xnew = max(0,max(x-move,min(1,min(x+move,(x.*sqrt(-
dc./dv/lmid)).^q))));
        xPhys(:) = (H*xnew(:))./Hs;
        if sum(xPhys(:)) > volfrac*nele, l1 = lmid; else l2 = lmid; end
    end
    change = max(abs(xnew(:)-x(:)));
    x = xnew;
    % PRINT RESULTS
    fprintf(' It.:%5i Obj.:%11.4f Vol.:%7.3f
ch.:%7.3f\n',loop,c,mean(xPhys(:)),change);
    % PLOT DENSITIES
    if displayflag, clf; display_3D(xPhys); end %#ok<UNRCH>
```

```
end
clf; display_3D(xPhys);
end


% === GENERATE ELEMENT STIFFNESS MATRIX ===
function [KE] = lk_H8(nu)
A = [32 6 -8 6 -6 4 3 -6 -10 3 -3 -3 -4 -8;
    -48 0 0 -24 24 0 0 0 12 -12 0 12 12 12];
k = 1/144*A'*[1; nu];

K1 = [k(1) k(2) k(2) k(3) k(5) k(5);
    k(2) k(1) k(2) k(4) k(6) k(7);
    k(2) k(2) k(1) k(4) k(7) k(6);
    k(3) k(4) k(4) k(1) k(8) k(8);
    k(5) k(6) k(7) k(8) k(1) k(2);
    k(5) k(7) k(6) k(8) k(2) k(1)];
K2 = [k(9)  k(8)  k(12) k(6)  k(4)  k(7);
    k(8)  k(9)  k(12) k(5)  k(3)  k(5);
    k(10) k(10) k(13) k(7)  k(4)  k(6);
    k(6)  k(5)  k(11) k(9)  k(2)  k(10);
    k(4)  k(3)  k(5)  k(2)  k(9)  k(12)
    k(11) k(4)  k(6)  k(12) k(10) k(13)];
K3 = [k(6)  k(7)  k(4)  k(9)  k(12) k(8);
    k(7)  k(6)  k(4)  k(10) k(13) k(10);
    k(5)  k(5)  k(3)  k(8)  k(12) k(9);
    k(9)  k(10) k(2)  k(6)  k(11) k(5);
    k(12) k(13) k(10) k(11) k(6)  k(4);
    k(2)  k(12) k(9)  k(4)  k(5)  k(3)];
K4 = [k(14) k(11) k(11) k(13) k(10) k(10);
    k(11) k(14) k(11) k(12) k(9)  k(8);
    k(11) k(11) k(14) k(12) k(8)  k(9);
    k(13) k(12) k(12) k(14) k(7)  k(7);
    k(10) k(9)  k(8)  k(7)  k(14) k(11);
    k(10) k(8)  k(9)  k(7)  k(11) k(14)];
K5 = [k(1) k(2)  k(8)  k(3) k(5)  k(4);
    k(2) k(1)  k(8)  k(4) k(6)  k(11);
    k(8) k(8)  k(1)  k(5) k(11) k(6);
    k(3) k(4)  k(5)  k(1) k(8)  k(2);
    k(5) k(6)  k(11) k(8) k(1)  k(8);
    k(4) k(11) k(6)  k(2) k(8)  k(1)];
K6 = [k(14) k(11) k(7)  k(13) k(10) k(12);
    k(11) k(14) k(7)  k(12) k(9)  k(2);
    k(7)  k(7)  k(14) k(10) k(2)  k(9);
    k(13) k(12) k(10) k(14) k(7)  k(11);
    k(10) k(9)  k(2)  k(7)  k(14) k(7);
    k(12) k(2)  k(9)  k(11) k(7)  k(14)];
KE = 1/((nu+1)*(1-2*nu))*...
    [ K1  K2  K3  K4;
    K2'  K5  K6  K3';
    K3' K6  K5' K2';
    K4  K3  K2  K1'];
end
% === DISPLAY 3D TOPOLOGY (ISO-VIEW) ===
function display_3D(rho)
```

```
[nely,nelx,nelz] = size(rho);
hx = 1; hy = 1; hz = 1;            % User-defined unit element size
face = [1 2 3 4; 2 6 7 3; 4 3 7 8; 1 5 8 4; 1 2 6 5; 5 6 7 8];
set(gcf,'Name','ISO display','NumberTitle','off');
for k = 1:nelz
    z = (k-1)*hz;
    for i = 1:nelx
        x = (i-1)*hx;
        for j = 1:nely
            y = nely*hy - (j-1)*hy;
            if (rho(j,i,k) > 0.5)  % User-defined display density threshold
                vert = [x y z; x y-hx z; x+hx y-hx z; x+hx y z; x y z+hx;x y-
hx z+hx; x+hx y-hx z+hx;x+hx y z+hx];
                vert(:,[2 3]) = vert(:,[3 2]); vert(:,2,:) = -vert(:,2,:);
                patch('Faces',face,'Vertices',vert,'FaceColor',[0.2+0.8*(1-
rho(j,i,k)),0.2+0.8*(1-rho(j,i,k)),0.2+0.8*(1-rho(j,i,k))]);
                hold on;
            end
        end
    end
end
axis equal; axis tight; axis off; box on; view([30,30]); pause(1e-6);
end
```

```
=========================================================================
% === This code was written by K Liu and A Tovar, Dept. of Mechanical   ===
% === Engineering, Indiana University-Purdue University Indianapolis,   ===
% === Indiana, United States of America                                 ===
% === ---------------------------------------------------------------- ===
% === Please send your suggestions and comments to: kailiu@iupui.edu    ===
% === ---------------------------------------------------------------- ===
% === The code is intended for educational purposes, and the details    ===
% === and extensions can be found in the paper:                         ===
% === K. Liu and A. Tovar, "An efficient 3D topology optimization code  ===
% === written in Matlab", Struct Multidisc Optim, 50(6): 1175-1196, 2014, =
% === doi:10.1007/s00158-014-1107-x                                     ===
% === ---------------------------------------------------------------- ===
% === The code as well as an uncorrected version of the paper can be    ===
% === downloaded from the website: http://www.top3dapp.com/             ===
% === ---------------------------------------------------------------- ===
% === Disclaimer:                                                       ===
% === The authors reserves all rights for the program.                  ===
% === The code may be distributed and used for educational purposes.    ===
% === The authors do not guarantee that the code is free from errors
```

A.2 STL conversion Matlab code (A simple STL writter for Top3d by Liu (Apr 2015) https://top3dapp.com [71])

```
function Top3dSTL_v3(fout, varargin)
%Top3dSTL_v3   A simple STL writter for Top3d by Liu (Apr 2015)
%   Top3dSTL_v3(fout) writes a STL file with name fout using cubic
%   representation and binary file format if xPhys exists in Workspace.
%
%   Top3dSTL_v3(fout, xPhys) writes a STL file with name fout using cubic
%   representation and binary file format
%
%   Top3dSTL_v3(___, Name, Value) writes a STL file with one or more Name,
%   Value pair argments. Use this option with any of the input argument
%   combinations in the prvious syntaxes.
%       FORMAT     - File is written in 'binary' (default) or 'ascii' format.
%       TITLE      - Header text (max 80 characters) written to the STL file.
%       MODE       - Facets are generated using 'cube' (default) or 'iso'.
%       CUTOFF     - Density cutoff value. default: 0.5
%       FACECOLOR  - Face color. default: 'cyan'
%       ALPHA      - Face alpha value. default: 1.
%       UNITLENGTH - Vector of element unit length. default: [1 1 1]
%       PLOT       - Logic flag to display structures. default: true
%
%   Example 1:
%       Top3dSTL_v3('MyTop3d.stl') % when xPhys is in Workspace
%
%   Example 2:
%       Top3dSTL_v3('MyTop3d.stl', density, ...
%       'Format', 'ascii', 'Mode', 'iso', 'FaceColor', 'm', 'Plot', false)
%

% Determine input type
if ~isempty(varargin) && (isnumeric(varargin{1}) || islogical(varargin{1}))
    xPhys = varargin{1};
    options = parseInputs(varargin{2:end});
else
    try
        xPhys = evalin('base', 'xPhys');
    catch ME
        switch ME.identifier
            case 'MATLAB:UndefinedFunction'
                error('xPhys is not input argument nor exist in workspace');
            otherwise
                rethrow(ME)
        end
    end
    options = parseInputs(varargin{:});
end

% Generate faces and verts
if strcmp(options.mode, 'cube')
    [faces, verts] = getCube(xPhys, options);
else
    [faces, verts] = getISO(xPhys, options);
end
```

```
% Facets
facets = single(verts);
facets = reshape(facets(faces',:)', 3, 3, []);
% facets: (:,:,1) --> Vertices of face 1,
% facets(:,1,1)   --> First vertice of face 1
V1 = squeeze(facets(:,2,:) - facets(:,1,:));
V2 = squeeze(facets(:,3,:) - facets(:,1,:));

% Normal vectors
normals = cross(V1, V2);
clear V1 V2
% Normal vectors normalization
normals = bsxfun(@times, normals, 1 ./ sqrt(sum(normals .* normals, 1)));

facets = cat(2, reshape(normals, 3, 1, []), facets);
clear normals

% Write STL
if strcmp(options.format, 'ascii')
    writeAscii(facets, fout, options.title);
else
    writeBinary(facets, fout, options.title);
end

end

function options = parseInputs(varargin)
OP = inputParser;
defaultFormat    = 'binary';
expectedFormat   = {'ascii', 'binary'};
defaultMode      = 'cube';
expectedMode     = {'cube', 'iso'};
defaultTitle     = sprintf('Created by Top3dSTL.m %s',datestr(now));
defaultCutoff    = 0.5;
defaultFcolor    = 'c';
defaultAlpha     = 1;
defaultUnitLegth = [1, 1, 1];
defaultPlot      = true;

OP.addParamValue('format', defaultFormat, ...
    @(x) any(validatestring(x,expectedFormat)))
OP.addParamValue('mode', defaultMode, ...
    @(x) any(validatestring(x,expectedMode)))
OP.addParamValue('title', defaultTitle, @ischar);
OP.addParamValue('cutoff', defaultCutoff, @isnumeric)
OP.addParamValue('facecolor', defaultFcolor, @ischar)
OP.addParamValue('alpha', defaultAlpha, @isnumeric)
OP.addParamValue('unitlength', defaultUnitLegth, ...
    @(x) validateattributes(x, {'numeric'}, {'vector'}));
OP.addParamValue('plot', defaultPlot, @islogical)

OP.parse(varargin{:});
options = OP.Results;
end
```

```
function [faces, verts] = getCube(xPhys, options)
% Generate Mesh
nx = options.unitlength(1);
ny = options.unitlength(2);
nz = options.unitlength(3);
[nely, nelx, nelz] = size(xPhys);
nele    = nelx*nely*nelz;
nodegrd = reshape(1:(nely+1)*(nelx+1),nely+1,nelx+1);
nodeids = reshape(nodegrd(1:end-1,1:end-1),nely*nelx,1);
nodeidz = 0:(nely+1)*(nelx+1):(nelz-1)*(nely+1)*(nelx+1);
nodeids = repmat(nodeids, size(nodeidz))+repmat(nodeidz, size(nodeids));
enodVec = nodeids(:)+1;
enodMat = repmat(enodVec,1,8)+ ...
    repmat([0 nely + [1 0] -1 ...
    (nely+1)*(nelx+1)+[0 nely + [1 0] -1]],nele,1);

% Faces connectivities
enodidx = [...
    1 3 2; 1 4 3; ... % back
    5 6 7; 5 7 8; ... % front
    1 5 8; 1 8 4; ... % left
    6 2 3; 6 3 7; ... % right
    8 7 3; 8 3 4; ... % up
    1 2 6; 1 6 5];    % down

faces = [];

% Filter out Low density
xPhys(xPhys < options.cutoff)  = 0;
xPhys(xPhys >= options.cutoff) = 1;

for f = 1:size(enodMat,1)
    if xPhys(f) == 0
        continue;
    end

    % Coordinates
    [j, i, k] = ind2sub([nely, nelx, nelz], f);
    eFace   = enodidx;      % element faces connectivities
    idx     = [];           % element faces to be deleted
    % Neighbor on back
    if (k ~= 1 && xPhys(j, i, k - 1) == 1)
        idx = [idx; [1 2]];
    end
    % Neighbor on front
    if (k ~= nelz && xPhys(j, i, k + 1) == 1)
        idx = [idx; [3 4]];
    end
    % Neighbor on left
    if (i ~= 1 && xPhys(j, i - 1, k) == 1)
        idx = [idx; [5 6]];
    end
    % Neighbor on right
```

```
    if (i ~= nelx && xPhys(j, i + 1, k) == 1)
        idx = [idx; [7 8]];
    end
    % Neighbor on up
    if (j ~= 1 && xPhys(j - 1, i, k) == 1)
        idx = [idx; [9 10]];
    end
    % Neighbor on down
    if (j ~= nely && xPhys(j + 1, i, k) == 1)
        idx = [idx; [11 12]];
    end

    eFace(idx, :) = [];
    tmp   = enodMat(f,:);
    faces = cat(1, faces, tmp(eFace));

end

% Vertices
[xx, yy, zz] = meshgrid(0:nx:nelx*nx, ...
    0:ny:nely*ny, ...
    0:nz:nelz*nz);
verts = [xx(:) nely-yy(:) zz(:)];

% Visualization
if options.plot
    dverts = [xx(:) zz(:) yy(:)];
    cla, hold on, view(30,30), rotate3d on, axis equal
    axis([0 nelx*nx 0 nelz*nz 0 nely*ny]), box
    set(gca,'YDir', 'reverse', 'ZDir', 'reverse', 'ZtickLabel',
flipud(get(gca, 'Ztick')'));
    patch('faces', faces, 'vertices', dverts, 'FaceColor', options.facecolor,
'FaceAlpha', options.alpha)
    xlabel('x'), ylabel('z'), zlabel('y')
end
end

function [faces, verts] = getISO(xPhys, options)
nx = options.unitlength(1);
ny = options.unitlength(2);
nz = options.unitlength(3);
[nely, nelx, nelz] = size(xPhys);

aux = zeros(nely+2, nelx+2, nelz+2);
aux(2:end-1,2:end-1,2:end-1) = xPhys;

[X,Y,Z] = meshgrid(0:nx:nx*(nelx+1), ...
    0:ny:ny*(nely+1), ...
    0:nz:nz*(nelz+1));

[faces, verts] = isosurface(X-0.5, Z-0.5, Y-0.5, aux, options.cutoff);

% Visualization
if options.plot
```

```
    cla, hold on, view(30,30), rotate3d on, axis equal
    axis([0 nx*nelx 0 nz*nelz 0 ny*nely]), box
    set(gca, 'YDir', 'reverse', 'ZDir', 'reverse', 'ZtickLabel',
flipud(get(gca, 'Ztick')'));

    patch('Faces', faces, 'Vertices', verts,...
        'FaceColor', options.facecolor, 'EdgeColor', 'none', 'FaceAlpha',
options.alpha);
    camlight, lighting gouraud;
    xlabel('x'), ylabel('z'), zlabel('y')
    drawnow
end
end

function writeAscii(facets, fout, title)
% Write ASCII STL file
%{
FORMAT:

solid name
    facet normal ni nj nk
        outer loop
            vertex v1x v1y v1z
            vertex v2x v2y v2z
            vertex v3x v3y v3z
        endloop
    endfacet
end solid name

%}
fid = fopen(fout, 'wb+');
fprintf(fid, [title, '\r\n']);
fprintf(fid,[...
    'facet normal %.7E %.7E %.7E\r\n' ...
    'outer loop\r\n' ...
    'vertex %.7E %.7E %.7E\r\n' ...
    'vertex %.7E %.7E %.7E\r\n' ...
    'vertex %.7E %.7E %.7E\r\n' ...
    'endloop\r\n' ...
    'endfacet\r\n'], facets);
fprintf(fid, ['end ', title, '\r\n']);
fclose(fid);
fprintf('Wrote %d facets to %s\n',size(facets, 3), fout);
end

function writeBinary(facets, fout, title)
% Write Binary STL file
%{
FORMAT:

UINT8[80] ? Header
UINT32 ? Number of triangles

foreach triangle
```

```
    REAL32[3] ? Normal vector
    REAL32[3] ? Vertex 1
    REAL32[3] ? Vertex 2
    REAL32[3] ? Vertex 3
    UINT16 ? Attribute byte count
end

%}
fid = fopen(fout, 'wb+');
fprintf(fid, '%-80s', title);                    % Title
fwrite(fid, size(facets, 3), 'uint32');          % Number of facets
facets = typecast(facets(:), 'uint16');          % Convert to unit16
facets = reshape(facets, 12*2, []);
facets(end+1, :) = 0;                            % Add color(0) to the end of
each facet
fwrite(fid, facets, 'uint16');
fclose(fid);
fprintf('Wrote %d facets to %s\n',size(facets, 2), fout);
end
```

A.3 Three point bending test simulation – INP file (Material properties, Boundary conditions)

**

** MATERIALS

**

*Material, name="SS 316l"

*Elastic

2.321e+07, 0.265

**

** INTERACTION PROPERTIES

**

*Surface Interaction, name=IntProp-1

1.,

*Friction, slip tolerance=0.005

0.1,

*Surface Behavior, pressure-overclosure=HARD

*Surface Smoothing, name=CP-1-Part-2-1-Taubin_Smoothing-new-1

, _CP-1-Part-2-1-Taubin_Smoothing-new-1_msm_1, CIRCUMFERENTIAL, 1.22175, -0.336883, -0.637795, 1.22175, -0.336883, 0.362205

, _CP-1-Part-2-1-Taubin_Smoothing-new-1_msm_2, CIRCUMFERENTIAL, 1.22175, -0.336883, -0.637795, 1.22175, -0.336883, 0.362205

*Surface Smoothing, name=CP-2-Part-2-1-Taubin_Smoothing-new-1

, _CP-2-Part-2-1-Taubin_Smoothing-new-1_msm_1, CIRCUMFERENTIAL, 1.22175, -0.336883, -0.637795, 1.22175, -0.336883, 0.362205

, _CP-2-Part-2-1-Taubin_Smoothing-new-1_msm_2, CIRCUMFERENTIAL, 1.22175, -0.336883, -0.637795, 1.22175, -0.336883, 0.362205

*Surface Smoothing, name=CP-3-Part-2-2-Taubin_Smoothing-new-1

, _CP-3-Part-2-2-Taubin_Smoothing-new-1_msm_1, CIRCUMFERENTIAL, 6.63976, -0.336883, -0.637795, 6.63976, -0.336883, 0.362205

, _CP-3-Part-2-2-Taubin_Smoothing-new-1_msm_2, CIRCUMFERENTIAL, 6.63976, -0.336883, -0.637795, 6.63976, -0.336883, 0.362205

*Surface Smoothing, name=CP-4-Part-2-2-Taubin_Smoothing-new-1

, _CP-4-Part-2-2-Taubin_Smoothing-new-1_msm_1, CIRCUMFERENTIAL, 6.63976, -0.336883, -0.637795, 6.63976, -0.336883, 0.362205

, _CP-4-Part-2-2-Taubin_Smoothing-new-1_msm_2, CIRCUMFERENTIAL, 6.63976, -0.336883, -0.637795, 6.63976, -0.336883, 0.362205

*Surface Smoothing, name=CP-5-Part-2-3-Taubin_Smoothing-new-1

, _CP-5-Part-2-3-Taubin_Smoothing-new-1_msm_1, CIRCUMFERENTIAL, 3.9517, 2.31058, -0.496889, 3.9517, 2.31058, 0.503111

, _CP-5-Part-2-3-Taubin_Smoothing-new-1_msm_2, CIRCUMFERENTIAL, 3.9517, 2.31058, -0.496889, 3.9517, 2.31058, 0.503111

**

** BOUNDARY CONDITIONS

**

** Name: BC-2 Type: Displacement/Rotation

*Boundary

Set-4, 1, 1

Set-4, 2, 2

Set-4, 3, 3

Set-4, 4, 4

Set-4, 5, 5

Set-4, 6, 6

** Name: BC-4 Type: Displacement/Rotation

*Boundary

Set-5, 1, 1

Set-5, 2, 2

Set-5, 3, 3

Set-5, 4, 4

Set-5, 5, 5

Set-5, 6, 6

**

** INTERACTIONS

**

** Interaction: CP-1-Part-2-1-Taubin_Smoothing-new-1

*Contact Pair, interaction=IntProp-1, type=SURFACE TO SURFACE, geometric correction=CP-1-Part-2-1-Taubin_Smoothing-new-1

CP-1-Taubin_Smoothing-new-1, CP-1-Part-2-1

** Interaction: CP-2-Part-2-1-Taubin_Smoothing-new-1

*Contact Pair, interaction=IntProp-1, type=SURFACE TO SURFACE, geometric correction=CP-2-Part-2-1-Taubin_Smoothing-new-1

CP-2-Taubin_Smoothing-new-1, CP-2-Part-2-1

** Interaction: CP-3-Part-2-2-Taubin_Smoothing-new-1

*Contact Pair, interaction=IntProp-1, type=SURFACE TO SURFACE, geometric correction=CP-3-Part-2-2-Taubin_Smoothing-new-1

CP-3-Taubin_Smoothing-new-1, CP-3-Part-2-2

** Interaction: CP-4-Part-2-2-Taubin_Smoothing-new-1

*Contact Pair, interaction=IntProp-1, type=SURFACE TO SURFACE, geometric correction=CP-4-Part-2-2-Taubin_Smoothing-new-1

CP-4-Taubin_Smoothing-new-1, CP-4-Part-2-2

** Interaction: CP-5-Part-2-3-Taubin_Smoothing-new-1

*Contact Pair, interaction=IntProp-1, type=SURFACE TO SURFACE, adjust=0.0, geometric correction=CP-5-Part-2-3-Taubin_Smoothing-new-1

CP-5-Taubin_Smoothing-new-1, CP-5-Part-2-3

** Interaction: Int-1

*Contact

*Contact Inclusions, ALL EXTERIOR

*Contact Property Assignment

 , , IntProp-1

*Surface Property Assignment, property=GEOMETRIC CORRECTION

_Int-1_gcs0_1, Circumferential, 1.22175, -0.336883, -0.637795, 1.22175, -0.336883, 0.362205

_Int-1_gcs0_2, Circumferential, 1.22175, -0.336883, -0.637795, 1.22175, -0.336883, 0.362205

_Int-1_gcs0_8, Circumferential, 1.22175, -0.336883, -0.637795, 1.22175, -0.336883, 0.362205

_Int-1_gcs0_9, Circumferential, 1.22175, -0.336883, -0.637795, 1.22175, -0.336883, 0.362205

_Int-1_gcs0_18187, Circumferential, 6.63976, -0.336883, -0.637795, 6.63976, -0.336883, 0.362205

_Int-1_gcs0_18188, Circumferential, 6.63976, -0.336883, -0.637795, 6.63976, -0.336883, 0.362205

_Int-1_gcs0_18194, Circumferential, 6.63976, -0.336883, -0.637795, 6.63976, -0.336883, 0.362205

_Int-1_gcs0_18195, Circumferential, 6.63976, -0.336883, -0.637795, 6.63976, -0.336883, 0.362205

_Int-1_gcs0_18201, Circumferential, 3.9517, 2.31058, -0.496889, 3.9517, 2.31058, 0.503111

_Int-1_gcs0_18202, Circumferential, 3.9517, 2.31058, -0.496889, 3.9517, 2.31058, 0.503111

_Int-1_gcs0_18208, Circumferential, 3.9517, 2.31058, -0.496889, 3.9517, 2.31058, 0.503111

_Int-1_gcs0_18209, Circumferential, 3.9517, 2.31058, -0.496889, 3.9517, 2.31058, 0.503111

** --

**

** STEP: Step-1

**

*Step, name=Step-1, nlgeom=NO, inc=10000

*Static, stabilize=0.0002, allsdtol=0.05, continue=NO

0.02, 1., 1e-08, 1.

**

** BOUNDARY CONDITIONS

**

** Name: BC-3 Type: Displacement/Rotation

*Boundary, amplitude=Amp-3

Set-6, 1, 1

Set-6, 2, 2, -0.00984252

Set-6, 3, 3

Set-6, 4, 4

Set-6, 5, 5

Set-6, 6, 6

**

** OUTPUT REQUESTS

**

*Restart, write, frequency=0

**

** FIELD OUTPUT: F-Output-1

**

*Output, field

*Node Output

CF, RF, RM, RT, TF, U, UR, UT

V, VF, VR, VT

*Element Output, directions=YES

ALPHA, ALPHAN, BF, CENTMAG, CENTRIFMAG, CORIOMAG, CS11, CTSHR, E, EE, ER, ESF1, GRAV, HP, IE, LE

MISES, MISESMAX, MISESONLY, NE, NFORC, NFORCSO, P, PE, PEEQ, PEEQMAX, PEEQT, PEMAG, PEQC, PRESSONLY, PS, ROTAMAG

S, SALPHA, SE, SEE, SEP, SEPE, SF, SPE, SSAVG, THE, TRIAX, TRNOR, TRSHR, TSHR, VE, VEEQ

VS

**

** HISTORY OUTPUT: H-Output-1

**

*Output, history

*Node Output, nset=Set-6

RF2, U2

*End Step